Coherence Analysis of the Space Launch System using Unsteady Pressure Sensitive Paint

Francesco Soranna*, Patrick S. Heaney†, Martin K. Sekula‡, David J. Piatak§, James M. Ramey¶
NASA Langley Research Center, Hampton, VA 23681

Transonic buffet forces are a major source of unsteady loading on launch vehicles, thus requiring accurate estimation for efficient vehicle design. The state of the art in modeling these unsteady loads utilizes wind-tunnel tests where the fluctuating pressures are measured by pressure transducers (PTs) at discrete locations on a rigid buffet model. These pressures are then integrated over the surface of the vehicle to yield a series of orthogonal centerline loads called buffet forcing functions (BFFs). Typically, the PT layout aims at resolving the pressure correlation along the longitudinal axis of the vehicle. As a result, the distribution of azimuthal correlation and its impact on the estimated BFFs are not well known. To fill these gaps, extremely high-spatial-resolution unsteady pressure sensitive paint (uPSP) data were collected for three different configurations of the Space Launch System in the NASA Ames Research Center 11-Foot Transonic Unitary Plan Wind Tunnel. The spatio-temporal behavior of the pressure correlation on these vehicles is analyzed and flow features of interest are investigated. It is shown that terminal shocks interacting with turbulence are a source of increased azimuthal coherence, especially when the shock develops at a vehicle junction. Vortex shedding off the forward attachment hardware that connects the core stage to the solid rocket boosters (SRBs) is the most severe buffet environment on the vehicle. The associated fluctuating pressures are shown to be highly coherent aft of the attachment and as far back as the vehicle tail and up to 40 degrees away from the boosters. For selected areas of the vehicle, factoring the azimuthal coherence into the attenuation of discrete-measurement-based BFFs results in underprediction relative to the BFFs obtained from full integration of the uPSP data.

Notice to Readers

The Space Launch System, including its predicted performance and certain other features and characteristics, have been defined by the U.S. Government to be Sensitive But Unclassified (SBU). Information deemed to be SBU requires special protection and may not be disclosed to an international audience. To comply with SBU restrictions, details such as absolute values have been removed from some plots and figures in this paper. It is the opinion of the authors that despite these alterations, there is no loss of meaningful technical content. Analytical methodologies and capabilities are discussed, significant and interesting technical results are still present, and meaningful conclusions are presented.

Acronyms

BFF	=	buffet forcing function
EUS	=	Exploration Upper Stage
FAH	=	Forward Attachment Hardware
FI	=	Full Integration
LOX	=	Liquid Oxygen
MPCV	=	Multi-Purpose Crew Vehicle
OML	=	Outer Mold Line
PT	=	pressure transducer

*Research Aerospace Engineer, Aeroelasticity Branch, AIAA Member
†Research Aerospace Engineer, Aeroelasticity Branch, AIAA Member
‡Senior Research Aerospace Engineer, Aeroelasticity Branch
§Assistant Branch Head, Aeroelasticity Branch, AIAA Senior Member
¶Research Aerospace Engineer, Aeroelasticity Branch, AIAA Member

LSRB / RSRB	=	Left / Right Solid Rocket Booster
SM	=	Service Module
TBL	=	turbulent boundary layer
uPSP	=	unsteady pressure sensitive paint
USA	=	Universal Stage Adapter

Nomenclature

D	=	core diameter
$\Delta C_{p,\text{rms}}$	=	root-mean-square of pressure coefficient (mean removed)
f	=	frequency
i	=	axis index
j, k	=	panel indices
k_x	=	longitudinal wavenumber
l_i	=	coherence lengths
n	=	triangular cell index
N	=	number of triangular cells within a panel
p	=	unsteady pressure
Q	=	dynamic pressure
St	=	Strouhal number based on the core diameter and the freestream velocity
t	=	time
x, y, z	=	longitudinal, lateral, and vertical axes of the vehicle
U_c	=	turbulence-convection velocity
U_∞	=	freestream velocity
α	=	angle of attack
β	=	sideslip angle
γ	=	coherence function
θ	=	body coordinate system azimuthal angle
φ	=	cross-spectrum phase angle
ρ	=	normalized cross-correlation coefficient
τ	=	correlation time delay
Δx	=	longitudinal separation between stations
$\Delta\theta$	=	azimuthal separation between stations
Φ^p	=	power spectral density of the pressure
ω	=	angular frequency
λ	=	wavelength

I. Background and Methodology

The development of accurate buffet forcing functions (BFFs) for reliable launch vehicle design has made steady progress over the past 20 years thanks to a number of transonic wind-tunnel tests associated with NASA's Constellation and Space Launch System (SLS) programs. During these tests, rigid buffet models (RBMs) were instrumented with pressure transducers at hundreds of locations on the model, from which the unsteady forces are derived.

A key to improving the accuracy of BFFs is the spatial density of pressure transducers. Buffet tests conducted at the Transonic Dynamics Tunnel at the NASA Langley Research Center increased the number of unsteady pressure transducers from 256, installed on the Ares I and I-X RBMs in 2007 [1], to over 470 sensors used during the SLS-10005 test in 2014 [2]. Concurrently, techniques to compute BFFs from discrete pressure measurements have become increasingly sophisticated (Refs.[3–5]). Yet, inherent limitations still exist, tied mostly to limited spatial resolutions of discrete sensors.

In recent years, rapid progress made in the application of unsteady pressure sensitive paint (uPSP) measurements [6] has opened up completely new avenues for BFF development. In the most recent SLS test utilizing high spatio-temporal resolution PSP, nearly 1 million pressure measurements were achieved. This test was conducted at the 11-Ft Transonic Wind Tunnel of the NASA Ames Research Center (see details in the next section). Compared to the few hundreds of

measurement locations using pressure transducers, uPSP data approaches a continuous approximation of the unsteady pressure field on the launch vehicle.

While the uPSP technique has yet to mature for vehicle-design support, it provides a compelling opportunity to answer some of the questions that discrete measurement techniques fail to provide. For example, what is the spatial distribution of the pressure correlation? What are the actual unsteady forces acting on the vehicle, i.e., free of discretization assumptions? How does the azimuthal coherence impact the calculation of discrete BFFs? The present work continues ongoing efforts (Refs.[7], [8]) to tackle some of these challenging questions. Ultimately, the desire is to improve the state of the art in BFF estimation.

A. Test program description

This paper presents results from two transonic wind-tunnel tests that employed the uPSP measurement technique. Both tests were conducted at the NASA Ames Research Center (ARC) Unitary Plan Wind Tunnel (UPWT). The first test, the SLS Ascent Unsteady Aerodynamics Test (AUAT), took place in November and December of 2017. The test article was a 4-percent scale forebody model of the SLS Block 1B crew configuration, shown in Fig. 1(a). Testing was conducted at conditions ranging between Mach 0.80 and 1.40 and angle of attack and sideslip orientations between ±6 degrees. In addition to 250 unsteady pressure transducers, this test was the second launch vehicle test campaign at the 11- by 11-foot Transonic Wind Tunnel (11-foot TWT) to employ a uPSP measurement technique to acquire extremely high-spatial-density unsteady-pressure data at sample rates up to 20kHz. Details of this measurement method are documented in Ref. [6].

The second test is the SLS Ascent Transient Aerodynamics Test (ATAT), conducted in August and September 2019. While this test involved both the 11-foot TWT and 9- by 7-foot Supersonic Wind Tunnel (9x7 SWT) at UPWT, uPSP data were only collected in the 11-foot TWT, on two SLS configurations: 1) the SLS Block 1 cargo for the Europa Clipper Science Mission 1 (SM-1), and 2) the SLS Block 1B cargo with a low-fineness ratio ogive payload fairing. Photographs of the 2.5-percent scale models of these two configurations are shown in Fig. 1(b)-(c). The Mach number conditions ranged from 0.70 to 1.40 and the attitude range was the same as that tested during AUAT. Table 1 summarizes the SLS configurations corresponding to these tests.

Table 1 Wind-tunnel tests and associated SLS configurations for uPSP testing at the 11- by 11-foot transonic test section of the NASA ARC Unitary Plan Wind Tunnel.

Test	Year	SLS configuration	geometric scale
AUAT	2017	Block 1B crew	4-percent
ATAT	2019	Block 1 cargo	2.5-percent
ATAT	2019	Block 1B cargo	2.5-percent

B. Methodology: the panel method

Detailed descriptions of the uPSP test setup and data processing tools can be found in Refs. [6, 9]. In the present work, extremely high spatial-resolution uPSP data are used to characterize the pressure correlation on the surface of the SLS models described in the previous section. A panel method approach is followed that consists of defining contiguous panels on the vehicle surface and spatially averaging a subset of the uPSP unsteady pressures over hundreds of measurement locations within each panel (details to follow). While, in principle, the correlation between unsteady pressures can be computed from the raw uPSP measurements, spatial averaging reduces the electronic shot noise present in the uPSP data [4]. Building on recent methodologies introduced by Ref. [8], the panel method can be broken down in the following steps:

1) The uPSP measurement locations and associated pressure time histories are stored in multizone structured grids.
2) These grids are used to construct triangular cells based on the connectivity relationship between nodes; the cell-normal vectors and areas are computed following standard procedures.
3) At each triangular cell, the uPSP-measured unsteady pressures are mapped from the nearest node to the centroid of the cell.
4) The triangular cell centroids are mapped onto panels defined by a set of longitudinal and azimuthal boundaries.
5) At each time t, the pressure coefficient C_p associated with each panel is computed as:

$$C_p(t) = \frac{1}{Q} \frac{\sum_{n=1}^{N} A_n p_n}{\sum_{n=1}^{N} A_n}, \tag{1}$$

where the summation is carried over the number N of triangular-cell centroids within each panel. In Eq. 1, Q is the dynamic pressure, A_n and p_n represent, respectively, the area of the n-th triangular cell and the pressure fluctuation (time average removed) acting on its centroid.

The present work focuses on the analysis of the core stage. As an example of the application of the panel method, the AUAT grid (containing only the core body) has 633,743 uPSP nodes that are used to construct 1,223,632 triangular cells. To compute the C_p using Eq. 1, 6,000 panels are defined by 100 uniformly spaced longitudinal stations on the core, divided into 60 evenly spaced azimuthal stations. The corresponding longitudinal and azimuthal resolutions are $\Delta x/D = 5.7\%$ and $\Delta\theta/2\pi = 1.7\%$. The same panel resolutions are maintained for the ATAT grids. As a reference, the body coordinate systems employed in this paper are shown in Fig. 2.

II. Results

A. Coherence between panels on the vehicle

An initial analysis of the coherence for the SLS Block 1B crew vehicle based on high-spatial-resolution uPSP data was conducted in Ref. [8]. It presented spatial distributions and spectral content of the longitudinal coherence along the forebody of the vehicle. The study highlighted a very good agreement between uPSP data and discrete pressure transducers, in terms of coherence function and correlation lengths along the vehicle. The present study continues the work in Ref. [8], extending the analysis to both the longitudinal and azimuthal coherence distributions.

The panel method introduced in Section I.B is utilized to compute the pressure-based magnitude-squared coherence, γ^2, between panels j and k as:

$$\gamma(\omega)^2 = \frac{\left|\Phi^p_{jk}(\omega)\right|^2}{\Phi^p_{jj}(\omega)\,\Phi^p_{kk}(\omega)}, \tag{2}$$

where p is the unsteady pressure acting on each panel, Φ is the cross-PSD between panels j and k, at the angular frequency ω. Equation 2 is evaluated using the MSCOHERE function in MATLAB, windowing the pressure time histories using a 2048-sample Hamming window with 50% overlap between windows. In the next subsections, using Eq. 2, the spatial and spectral distribution of γ^2 is investigated for different buffet environments.

In the discussion that follows, specific buffet frequencies will be described in terms of a Strouhal number, $\mathrm{St} = fD/U_\infty$, where f is the frequency, D is the vehicle core diameter, and U_∞ is the freestream velocity. To aid the discussion, low buffet frequencies are defined in the St<0.5 range, intermediate in the range 0.5<St<1.0, and high for St>1.0.

1. Shock environments

Figure 3 shows sample unwrapped, root-mean-square (rms) distributions of $\Delta C_{p,\mathrm{rms}}$ (top chart) and γ^2 (bottom chart) on the Universal Stage Adapter (USA) of the Block 1B crew vehicle. Note that prior to computing the rms values, the time average is subtracted from the pressure time histories. The Mach number is 0.80 and the vehicle is at zero degrees attitude. The γ^2 distributions are obtained from Eq. 2, setting a reference panel, j = ref, and varying the index k within plus and minus one core diameter along the longitudinal direction, and ±90 degrees azimuthally. The magnitude-squared coherence values are plotted for a sample frequency corresponding to St=0.20. In the region under investigation, at this St number, relatively high γ^2-levels are found along both x and θ (further discussion to follow). The reference panel is located forward of the junction between the USA and the Exploration Upper Stage (EUS), as marked on the OML in Fig. 3.

Near the reference panel, Mach number contours from steady CFD simulations (see Fig. 4), show a rapid flow acceleration around the USA junction followed by a terminal shock aft of the USA junction. As seen in the contour plots of $\Delta C_{p,\mathrm{rms}}$ (Fig. 3, top chart), the shock location is highly unsteady relative to the surrounding environment, due to interaction of the shock with turbulence. In the same contour plot, note the presence of distinct azimuthal bands

of lower $\Delta C_{p,\mathrm{rms}}$ upstream of the shock, for example at $\Delta x/D < 0.13$ and $30 < \Delta\theta < 60$ degrees. As discussed in Ref. [10], these bands correspond to regions where the field of view of two uPSP cameras overlap. Combining data from two cameras reduces the measurement noise in the data and, consequently, the $\Delta C_{p,\mathrm{rms}}$ levels are reduced.

The γ^2 distribution (Fig. 3, bottom chart) reveals that, at this St number, the pressure coherence extends over a wide azimuthal region, comparable to the extent of the longitudinal coherence. This result is in contrast with, e.g., simulations of the wall pressure under turbulent boundary layers (Ref. [11]), that the cross stream coherence extends over a relatively narrow region. Analysis of the longitudinal and azimuthal coherence lengths, l_x and l_θ (not shown for brevity), reveals that, in the low frequency range (St<0.5, as defined in Section II.A), l_θ increases in closer proximity to the shock and, just downstream of the shock, l_θ even exceeds l_x (see also Section II.A.3). One last interesting aspect in Fig. 3 is that the $\gamma^2 \sim 0.50$ contour is not aligned with the x-axis (x=longitudinal direction), despite the vehicle attitude being at zero degrees.

A similar shock-related buffet environment exists in the Block 1B cargo configuration, where a terminal shock is responsible for increased $\Delta C_{p,\mathrm{rms}}$ on the Payload Fairing (Fig. 5). However, unlike the Block 1B crew configuration, where the shock is constrained at the USA-EUS junction (Fig. 3), for the Block 1B cargo, at the condition presented in Fig. 5 (Mach=0.95), the terminal shock is free to oscillate over a wider longitudinal region. As a result, broader longitudinal areas of high $\Delta C_{p,\mathrm{rms}}$ values are seen near this shock compared to the Block 1B crew counterpart. Another noticeable feature in the $\Delta C_{p,\mathrm{rms}}$ distribution of Fig. 5 are horizontal streaks located at $0<\Delta\theta<30$ and $150<\Delta\theta<180$ degrees. These relatively high pressure-fluctuation regions originate upstream, at the payload-fairing nose, and amplify through the normal shock (Ref. [12]).

Analysis of the coherence-lengths (not shown) across the Block 1B cargo terminal shock, indicates a frequency range corresponding to 0.02<St<0.1 where $l_x > l_\theta$. A sample γ^2 distribution within this range is shown in Fig. 5 (bottom chart), at St=0.07. In this case, the azimuthal coherence extends over a smaller region compared to the Block 1B crew case (Figure 3). This smaller region is potentially due the payload fairing being constant diameter, thus allowing the shock to oscillate more longitudinally.

2. Forward attachment hardware environment

The most severe buffet-environment on the SLS vehicle is located downstream of the Forward Attachment Hardware (FAH) that connects the solid rocket boosters (SRBs) to the core stage (Fig. 6). Highly-coherent vortex shedding off the FAH results in propagation of vortices down the length of the vehicle, causing significant pressure fluctuations on the SRBs and on the core. A striking animation of this phenomenon, based on the uPSP data presented in this paper, can be found at `https://www.nasa.gov/feature/ames/from-wind-to-data-in-no-time-flat-accelerating-spacecraft-and-aircraft-design/`. As pointed out in Ref. [2], the FAH environment is very sensitive to the geometry of the attachment hardware and, for specific designs, is a source of reduced structural margins.

Figures 7 and 8 show, respectively, distributions of $\Delta C_{p,\mathrm{rms}}$ and γ^2 on the Block 1 cargo core stage, within ±1 core diameters from a reference panel located just downstream of FAH (see OML at the bottom of Fig. 7), at transonic Mach numbers. Note that the magnitude-squared coherence contours of Fig. 8 are shown at the Strouhal number for vortex shedding of the FAH: St = 0.51 at Mach = 0.84, St = 0.34 at Mach = 0.91, and St = 0.54 at Mach = 1.10. In this figure, regions of obstructed uPSP optical access on the core are grayed out. Peak $\Delta C_{p,\mathrm{rms}}$ (Fig. 7) are observed around the SRBs and on the liquid oxygen (LOX) feedlines located on opposite sides of the core. These environments are most elevated at Mach=0.91 where the $\Delta C_{p,\mathrm{rms}}$ peak-levels are double those associated with the shock-related environments of the Block 1B crew and cargo configurations presented in Figs. 3 and 5 (note the difference in $\Delta C_{p,\mathrm{rms}}$ contour scales between Figs. 7 and e.g., Fig. 3). The corresponding distributions of γ^2 taken at the Strouhal number for vortex shedding (Fig. 8), highlight significant coherence both in the longitudinal and azimuthal direction. At nonzero values of angle of attack (Fig. 9), both $\Delta C_{p,\mathrm{rms}}$ and γ^2 contours are skewed toward the leeward side of the core, as expected.

3. Magnitude-squared coherence spectral content

The γ^2 distributions discussed in the previous sections were limited to specific frequencies corresponding to largest coherence within the shock and FAH environments. In the next paragraphs, the spectral content of γ^2 for these environments is analyzed along both the longitudinal and azimuthal directions.

Shock environment Focusing on the Block 1B crew vehicle, the γ^2 contour plots of Fig. 10 (bottom of the figure) provide distributions of azimuthal coherence, $\gamma^2(\Delta\theta, \omega \mid x = \mathrm{const})$, for three reference panels located: (1) upstream of the USA-EUS terminal shock, (2) in closer proximity to the shock, and (3) just downstream of it. The centroids of the

reference panels are marked on the OML in the middle of Fig. 10, and the $\Delta C_{p,\mathrm{rms}}$ contour plot at the top of the figure helps identify their position relative to the shock. Comparing the contour plots of γ^2 from the left to the right, the low frequency azimuthal coherence increases from the upstream side of the shock (panel 1) to the downstream side (panel 3). This frequency range, marked by a red-dash box on the γ^2 contour plot for panel-3, corresponds to St≤0.50.

The present data offer an opportunity to shed light on the rate of decay of the azimuthal coherence near a terminal shock, a quantity of interest for coherence modeling. Figure 11 presents profiles of $\gamma^2(\Delta\theta)$ corresponding to horizontal slices of the γ^2 contour plots of Fig. 10, taken at St=0.20, i.e., within the low frequency range. For simplicity, $\Delta\theta$ is limited to positive values. While on the upstream side of the shock (panel 1), $\gamma^2(\Delta\theta)$ is characterized by an exponential decay, on the downstream side, the decay rate is slower, approximately linear. Remarkably, relatively high coherence levels exist up to $\Delta\theta \sim 60$ degrees from the reference panel.

FAH environment Figure 12 presents distributions of longitudinal coherence as function of model-scale frequency, over a sample longitudinal segment extending ±1 core diameters from a reference panel in proximity to the Block 1 cargo FAH. The location of the sample segment is shown on the OML at the bottom of Fig. 12, along with the centroid of the reference panel. The normalized distance $\Delta x/D$ is measured from the centroid of the reference panel. The contour plots of Fig. 12 show the expected γ^2 decay with $\Delta x/D$, with the exception of the FAH vortex shedding frequency and its first harmonic (see dashed-red lines in Fig. 12), at which $\gamma^2 \sim 1$ levels persist well beyond $\Delta x/D > 1$. The Mach=0.91 condition clearly highlights an overall coherence increase in the mid to low frequency range, which is most important for buffet.

To highlight the extent of the vortex-shedding coherence, Fig. 13 presents slices of the contour plots of Fig. 12 at discrete $\Delta x/D$ points across the sample segment, including $\Delta x/D > 1$ locations, at Mach=0.91. The uPSP-panel centroids corresponding to the sample-points are marked on the OML on the left of Fig. 13. For as far as $\Delta x/D = 3.6$, the coherence at the vortex shedding frequency and its first harmonic (marked by dashed-black lines in Fig. 13) maintains significant levels. In Fig. 13, for reference, the uPSP-based γ^2 is compared to the magnitude-squared coherence based on pressure transducers instrumented at the same locations as the panels centroids shown on the OML. As previously shown in Ref. [8], excellent agreement between uPSP and pressure transducer (PT) coherence levels are observed over the frequency spectrum.

Moving on to the azimuthal coherence, Fig. 14 illustrates the variation of γ^2 with frequency and θ along an arc behind the Block 1 cargo FAH. The reference-panel centroid, indicated on the OML in Fig. 14, is the same as that in Fig. 12, i.e., the longitudinal and azimuthal coherence plots (Figs. 12 and 14) share the same origin. Note that at $\Delta\theta > 11$ degrees, uPSP data are lacking due to optical obstruction by the LSRB. Frequencies at and below the FAH vortex shedding frequency display elevated coherence out to $\Delta\theta \sim -20$ degrees at Mach=0.91. At this Mach number, an interesting feature observed at low frequencies is an increase in azimuthal coherence toward the LSRB ($\Delta\theta > 0$). At the highest Mach number (Mach=1.10), the Strouhal-shedding coherence extends out to $\Delta\theta \sim -30$ degrees, as seen also in the contour plots of Fig. 8, and its first harmonic strengthens significantly.

B. Cross correlation and convection velocity

In the context of coherence modeling of turbulent boundary layers (TBL), a key quantity is the turbulence-convection velocity, U_c (Ref.[13]). In this section, uPSP data are utilized to estimate U_c and a comparison to PT data is drawn. A common estimation method consists of the following steps (Ref. [14]):

1) compute the cross-correlation coefficient, ρ, between fluctuating pressures measured at fixed Δx separation.
2) Utilizing ρ computed in step 1), evaluate the time delay, τ, that corresponds to the peak ρ.
3) Compute $U_c = \Delta x/\tau$.

A similar U_c estimation technique was recently employed by Ref. [15] to estimate the convection velocity on the SLS Block 1 crew configuration.

Focusing on the Block 1 cargo FAH environment, Figure 15 presents plots of uPSP-based cross correlation (red curves) between a reference and sample panels, at Mach=0.91. The locations of these panels were previously introduced in Fig. 13. For comparison, the blue curves provide PT-based ρs at locations nearest the sample panels-centroids. Note that ρ is normalized so that the auto correlations at zero time delay are equal to one (according to the XCORR function in MATLAB). For each set of plots, the symbols correspond to the peak absolute values of ρ based on uPSP (red stars) and PT data (blue stars). As expected, the ρ peaks shift to larger values of τ with distance from the reference panel. Although trends of cross correlations from the two data sources are in good agreement, at certain panel locations, i.e., $\Delta x/D = 0.91$ and $\Delta x/D = 1.83$, the uPSP-based time delays underestimate their PT counterparts. The implication of

this will be clear shortly.

Figure16 shows the ratio of convection to freestream velocity, U_c/U_∞, estimated using uPSP and PT data at the panel locations of Figure 15. Additional uPSP-based data fill in the points between the sample panels of Fig. 15. Note that these additional points are sampled at the same azimuthal plane as the sample panels. Overall, the two data sources estimate convection velocities in the same range, e.g., $U_c/U_\infty \sim 0.55$ at $\Delta x/D = 1$. However, the uPSP data have some scatter, especially in the range $1 < \Delta x/D < 2$, where uPSP overestimates the PT-based convection velocities, a consequence of the mismatch in time delays pointed out in the previous paragraph (see Fig. 15). To understand the source of scatter, future analysis will focus on the sensitivity of the uPSP-based convection velocity to the location of the uPSP panels.

Moving on to the azimuthal correlation, Fig. 17 shows the cross correlation on the Block 1 cargo core stage along the arc shown in Fig. 14, at Mach=0.91. Consistent with the contour plots of γ^2 (Fig. 14), some level of correlation exist out to $\Delta\theta \sim -30$ degrees from the reference panel. A final note is that, as observed in Ref. [14], at this condition (Mach=0.91 and zero degrees attitude) the lack of delay time between azimuthally-spaced points implies that the fluctuating pressures act in phase along θ. In the next section, the analysis of the cross-spectrum phase will further elucidate this point.

C. Cross-spectrum phase

In this section, high-spatial density uPSP data are used to characterize the spatial distribution of the cross-spectrum phase angle, $\varphi^p_{jk}(\omega)$, between uPSP panels. Figure 18 provides plots of φ as a function of the model-scale frequency at sample panels on the Block 1 cargo core stage. The reference panel and the sample panels are those utilized in Fig. 13. All of the analysis presented here corresponds to Mach=0.91. In Fig. 18, PT-based φ are also included, showing an excellent agreement to the uPSP-derived data.

The φ plots reveal a sawtooth-like distribution, with the bandwidth of each ramp reducing with increased $\Delta x/D$, i.e., $d\varphi/df$ steepens away from the reference panel (f represents frequency). To get a better understanding of these trends, the contour plot of Fig. 19 shows the spectral distribution of φ along a longitudinal segment shown on the OML at the bottom of the figure. Note that each set of plots in Fig. 18 corresponds to $\Delta x/D$=constant slices of the contour plot of Fig. 19. In the contour plot, constant phase-angle contours follow a hyperbolic-like distribution with Δx and frequency. At larger distance from the reference panel, these isophase contours (Fig. 19) tend to collapse over a narrower frequency range, i.e., the phase-angle gradients $d\varphi/df$ get steeper. Steepening of $d\varphi/df$ occurs because the convection velocity is related to $d\varphi/df$ through (Ref. [16]):

$$U_c = 2\pi\Delta x(d\varphi/df)^{-1}, \tag{3}$$

where Δx is the separation between two pressure sample points. Thus, in order for the convection velocity to remain constant with distance (Fig. 16), the slope of $d\varphi/df$ increases away from the reference panel (Figs. 18).

An important observation based on Fig. 18 is that, at each $\Delta x/D$, a broad range of frequencies share the same $d\varphi/df$, i.e., convection velocity. Since $U_c = f\lambda = \omega/k_x$ (λ and k_x represent, respectively, the wavelength and the longitudinal wavenumber), multiple turbulent scales are advected at the same velocity, thus supporting Taylor's "frozen" turbulence hypothesis [17, 18], in the region under consideration. Note that because $-180 \leq \varphi \leq 180$ degrees, each phase-angle plot of Fig. 18 show several phase-angle ramps sharing the same slope.

A noticeable low-frequency feature in the isophase contours of Fig. 19 is a pair of discontinuities at $\Delta x/D = 4.0$ and $\Delta x/D = 4.5$. The first discontinuity is likely associated with vortex shedding off the aft attachment hardware connecting the SRBs to the core stage and located approximately at $\Delta x/D = 4.0$ in Fig. 19. As shown in Ref. [5], this region is characterized by pressure fluctuations that are highly coherent over the entire spectrum, especially at low frequencies. The second discontinuity ($\Delta x/D = 4.5$) is likely related to an OML change between the aft end of the core stage and the "boat-tail" shaped structure covering the core engines.

To shed light on the azimuthal distribution of the phase angle, Fig. 20 shows contours of φ along the longitudinal and azimuthal axes on the Block 1 cargo core stage for several Strouhal numbers, including that of vortex shedding (St=0.34). In each plot, Δx and $\Delta\theta$ are taken from a reference panel shown on the OML at the bottom of the figure. It is worth emphasizing that with the high spatial-resolution uPSP data, the phase angle approaches its continuous limit, i.e., $\varphi^p_{jk}(\omega) \sim \varphi^p(\Delta x, \Delta\theta|\omega)$. Several interesting features are noticeable: 1) at the lower Strouhal numbers, i.e., lower frequencies, regions of constant phase angle span almost the entire core (see St=0.04 case); 2) at higher frequencies, these wave fronts span a smaller $\Delta\theta$ (see St=0.72); 3) with increasing frequency or distance (from the reference panel) the phase-angle distributions become random, as expected from dissipation of smaller turbulent structures.

D. Buffet forces on panels

Recently, Soranna et al. [8] conducted a study on the impact of different coherence-based methods to SLS BFFs estimated from discrete pressure measurements. These BFFs were compared to higher-fidelity BFFs from full integration (FI) of high-spatial-resolution uPSP data. It was shown that frequency-dependent coherence factors do a very good job at estimating FI BFFs at low frequency (St<0.5, see Section II.A), where most of the buffet energy is contained. That study was limited to using longitudinal coherence factors, i.e., it did not account for the effect of azimuthal coherence on BFF attenuation. The latter is the subject of the present work.

Figure 21 illustrates the location of a sample BFF-integration panel on the Block 1 cargo core stage, spanning $\Delta\theta = 90$ degrees. The integration boundaries (solid lines) are taken from an actual SLS BFF database. The dashed lines illustrate a 22.5 degree integration panel, sharing the same longitudinal boundaries as the former. Power spectral densities, Φ_z^F, of the z-component of the unsteady force, F, acting on the integration panel are presented in Fig. 22, for both the 90-degrees (top) and 22.5-degrees (bottom) cases, at Mach=0.91. Each plot includes three sets of curves: (1) discrete BFFs with longitudinal coherence factors (red), (2) discrete BFFs with longitudinal and azimuthal coherence factors (purple), and (3) the FI BFFs (green). All the BFFs, discrete and FI BFFs, are obtained from uPSP data.

Focusing on the 90-degree integration panel (Fig. 22, top), the high-fidelity FI BFFs (green) are bounded from above by the discrete BFFs with longitudinal coherence factors (red). Including azimuthal integration factors (purple) results in underprediction of the higher-fidelity BFFs. When the azimuthal span of the integration panel is reduced (see 22.5-degree integration panel in Fig. 21), inherently, the discrete BFFs provide a better approximation to the FI BFFs. However, the discrete BFFs with longitudinal and azimuthal coherence factors (purple) continue to underestimate the FI BFFs at mid to high frequencies. At low frequencies, the azimuthal coherence factors provide no attenuation, because the azimuthal coherence lengths (not shown) associated with these low frequencies exceed the arclength of the integration panel.

Very similar conclusions are drawn based on a $\Delta\theta = 45$ degree BFF-integration panel located on the Block 1B cargo payload fairing (see solid lines on the OML of Fig. 5). For this integration panel, Figure 23 presents Φ_z^F comparisons between discrete and FI BFFs, at Mach=0.95. As in the previous case, including azimuthal coherence factors results in underestimation of the FI BFFs over almost the entire spectrum.

III. Conclusions

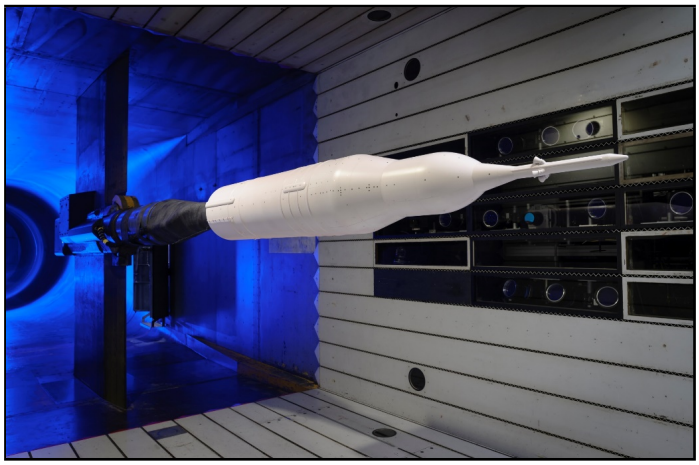
An analysis of the spectral and temporal behavior of the pressure correlation on the Space Launch System (SLS) is presented based on transonic wind-tunnel test data. Extremely high-spatial-density uPSP data are utilized, providing details of the buffet pressures at unprecedented resolutions, approaching 1 million uPSP measurement points. Data were collected on three SLS vehicle designs: the Block 1 cargo, the Block 1B crew, and Block 1B cargo configurations. Areas of the vehicle subject to different flow phenomena are investigated. Emphasis is given on the region behind the forward attachment hardware that connects the core stage to the solid rocket boosters (SRBs). This region experiences the most severe buffet environment on the vehicle - a concern for structural design. The same region also provides the highest signal-to-noise ratio (SNR) for uPSP measurements, a direct consequence of the high unsteady pressures there.

On the Block 1B crew configuration, a terminal shock develops at the junction between the Universal Stage Adapter (USA) and the Exploration Upper Stage (EUS). Interaction with turbulence makes this shock unsteady, although the shock motion is localized due to the USA-EUS junction. Relative to a reference location on the shock, the flow is highly coherent along the longitudinal direction as well as in the azimuthal direction, spanning almost 180 degrees. For comparison, another terminal shock is analyzed, the one that develops on the Block 1B cargo payload faring. Although this shock is also unsteady, within a low frequency range, the pressure coherence aligns more longitudinally, as a result of the shock moving unconstrained over a constant-radius payload fairing at the condition analyzed (Mach=0.95).

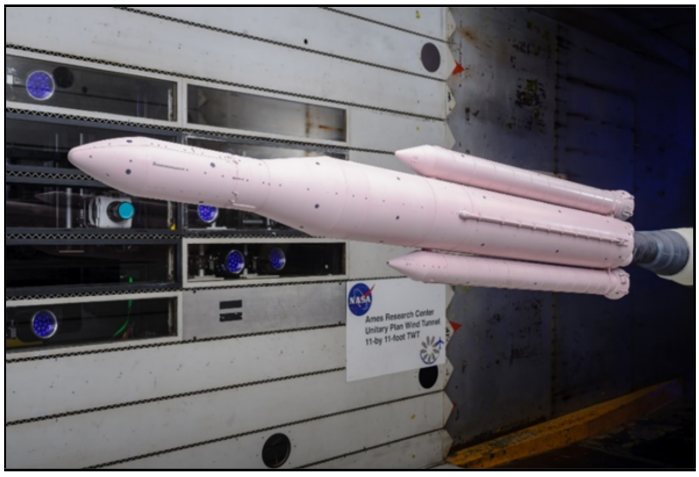
Behind the forward attachment hardware, $\Delta C_{p,\mathrm{rms}}$ levels associated with vortex shedding are double those measured near the terminal shock environments. At the vortex shedding frequency, the unsteady pressure on the core stage is highly coherent all the way to the vehicle tail. At this frequency, the azimuthal coherence on the core stage is also significant, extending up to 40 degrees away from the boosters. Lower frequencies below the Strouhal shedding (St<0.34 at Mach=0.91), also exhibit high azimuthal coherence, especially at Mach=0.91 where the magnitude-squared coherence is increased near the SRBs. As expected, a nonzero angle of attack causes the coherence to increase on the leeward side of the vehicle and decrease on the windward side. The uPSP-based correlation function is in very good agreement with pressure transducer data, thanks to high SNR. Consequently, trends of convection velocity, estimated from cross correlation, agree well between uPSP and PT data. However, the uPSP-based convection velocities present some scatter, possibly due to more sensitivity to local flow conditions.

The extremely high uPSP-measurement density provides new insights into the spatial distribution of cross-spectrum phase angle. On the core stage, at very low frequencies, constant phase-angle contours line up along the azimuthal direction, consistent with downstream propagation of low wave-number pressure modes. With higher frequencies and greater distance from a given source, these patterns become less organized and eventually randomly distributed. In the region behind the forward attachment hardware, the phase angles computed from uPSP and PT data are in excellent agreement.

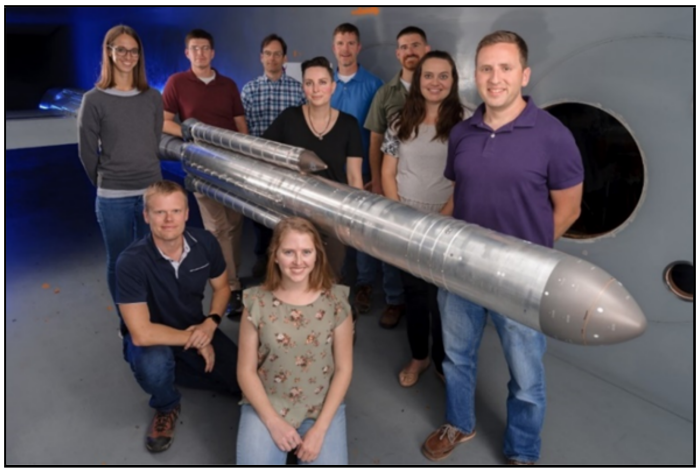
Finally, the attenuation of discrete-measurement-based BFFs is investigated utilizing longitudinal and azimuthal coherence factors. For selected integration panels on the core stage, when both factors are applied, discrete BFFs underestimate those obtained from full integration of the uPSP data. On the other hand, attenuating the BFFs with longitudinal coherence factors alone tends to be conservative, especially at higher frequencies. Future studies will focus on understanding the impact of the phase angle to BFF estimation based on discrete pressure measurements.



(a) SLS Block 1B crew 4-percent scale model tested during AUAT



(b) SLS Block 1 cargo 2.5-percent scale model tested during ATAT



(c) SLS Block 1B cargo 2.5-percent scale model tested during ATAT

Fig. 1 SLS RBMs and one of the ATAT crew teams at Ames UPWT.

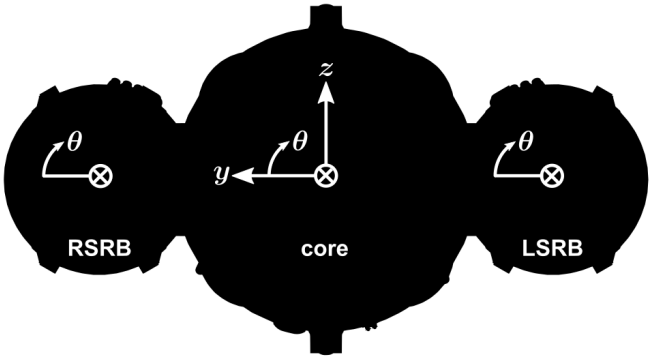


Fig. 2 Body coordinate systems on the core and on the left/right side solid rocket boosters, LSRB/RSRB. View in the aft-facing, $+x$, direction.

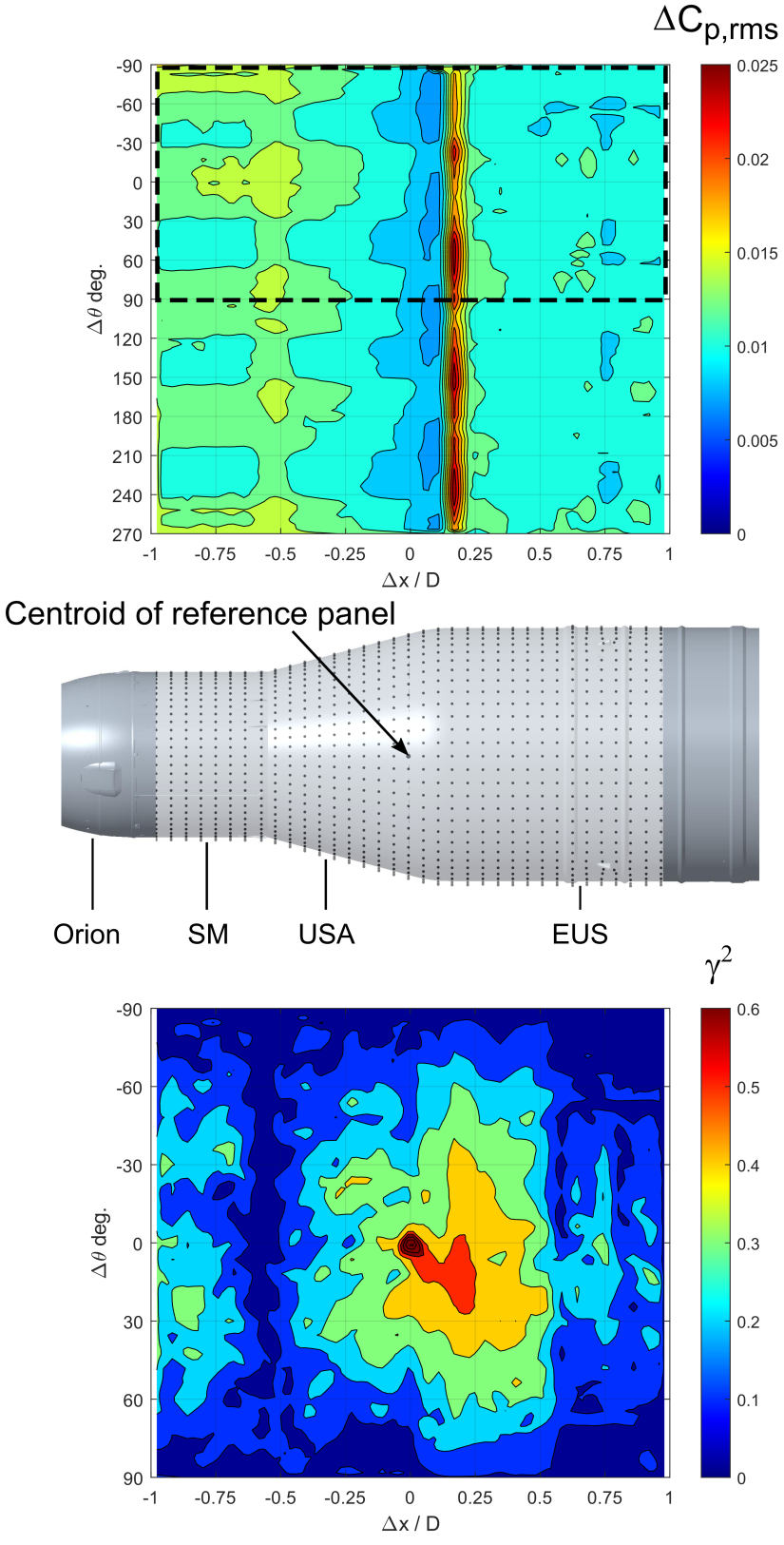


Fig. 3 Distributions of $\Delta C_{p,\mathrm{rms}}$ (top) and γ^2 (bottom) at St = 0.20 for a reference panel on the Block 1B crew Universal Stage Adapter. Also shown, the centroids of the uPSP panels overlaid on the OML of the vehicle (middle) and the boundaries of the γ^2 coherence region (dashed lines) on the distribution of $\Delta C_{p,\mathrm{rms}}$. Data for Mach = 0.80, $\alpha = 0$ deg, $\beta = 0$ deg.

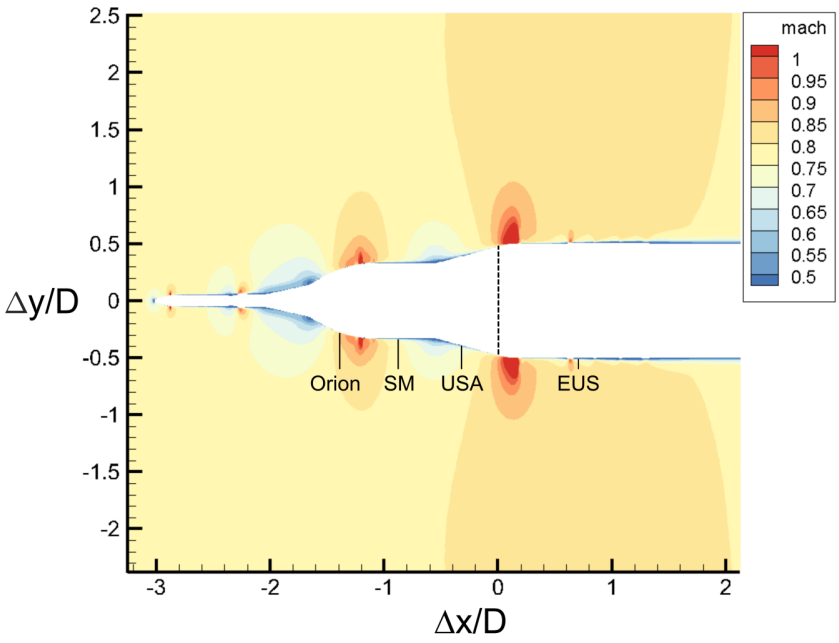


Fig. 4 Mach number distribution around the forebody of the Block 1B crew vehicle. The dashed line indicates the longitudinal plane containing the reference-panel centroid shown in Fig. 3 for Mach = 0.80, $\alpha = 0$ deg, $\beta = 0$ deg.

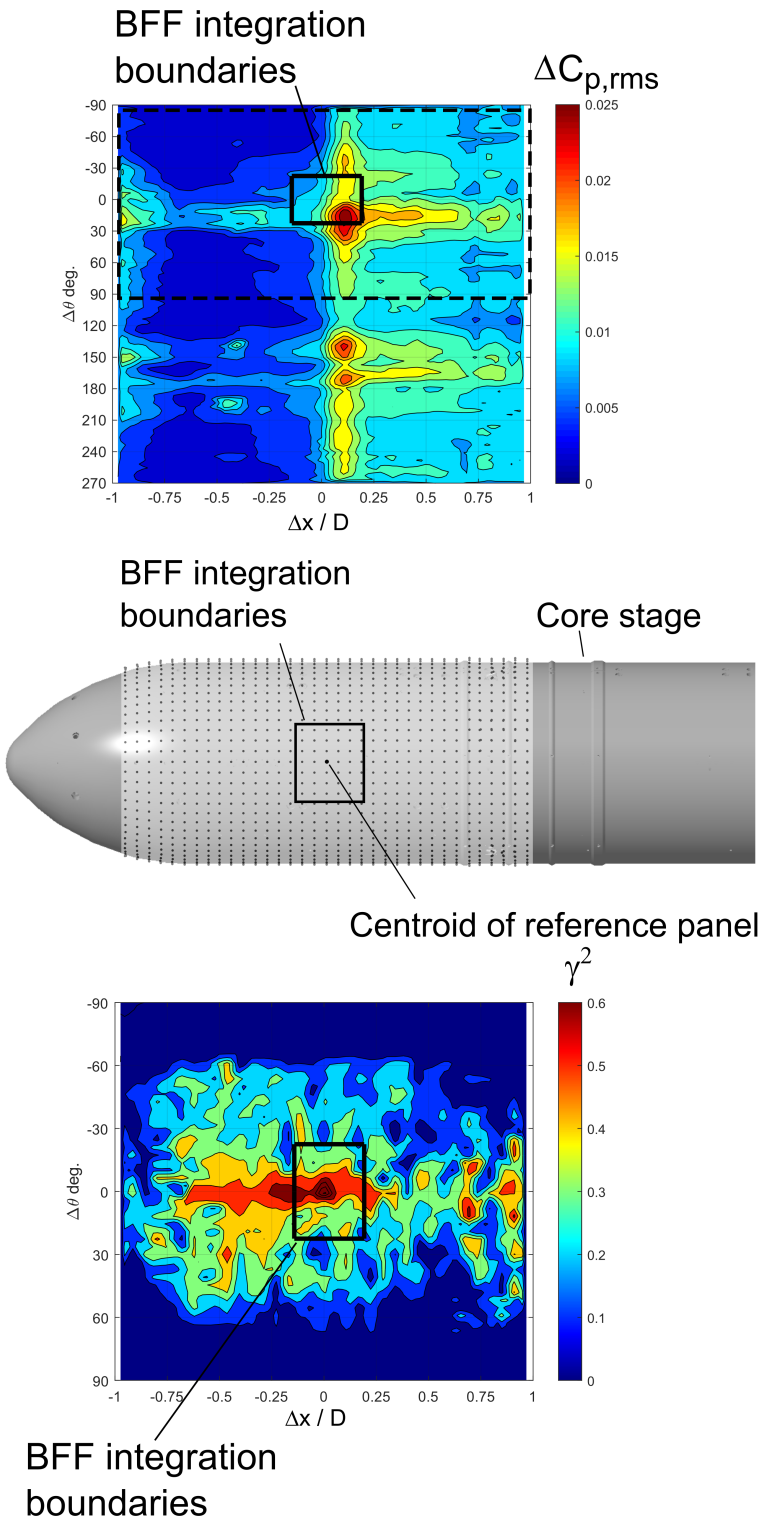


Fig. 5 Distributions of $\Delta C_{p,\mathrm{rms}}$ (top) and γ^2 (bottom) at St = 0.07 for a reference panel on the Block 1B cargo Payload Fairing. Also shown, the centroids of the uPSP panels overlaid on the OML of the vehicle (middle) and the boundaries of the γ^2 coherence region (dashed lines) on the distribution of $\Delta C_{p,\mathrm{rms}}$ for Mach = 0.95, $\alpha = 0$ deg, $\beta = 0$ deg.

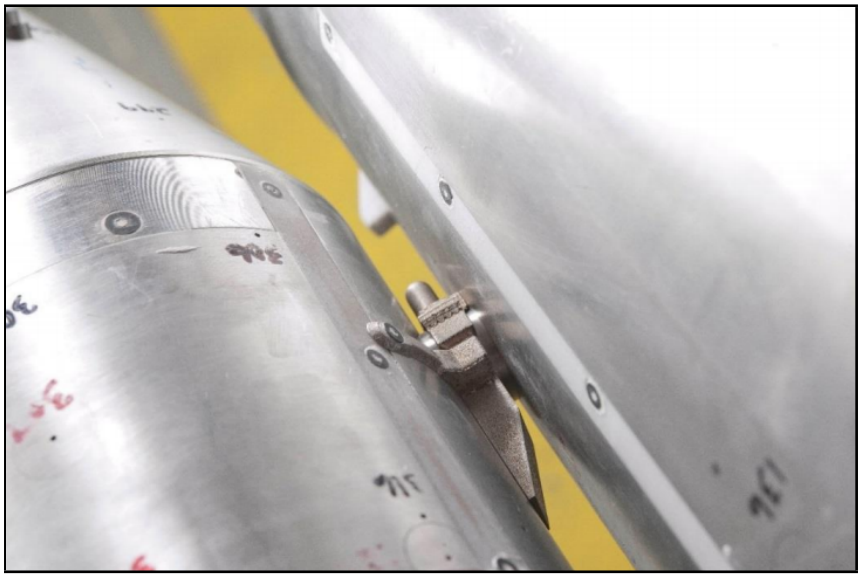


Fig. 6 Booster forward attachment hardware.

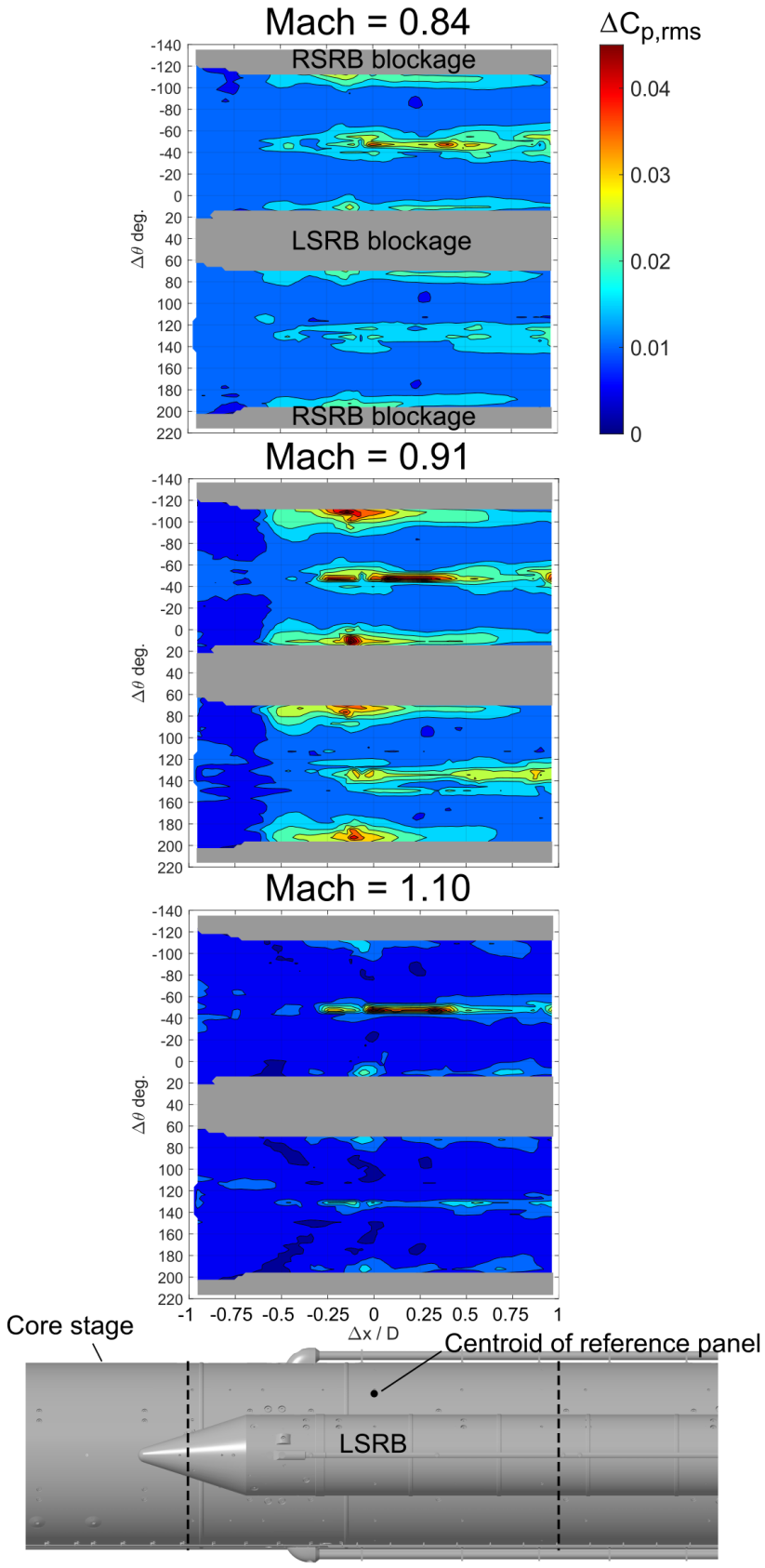


Fig. 7 Distributions of $\Delta C_{p,\mathrm{rms}}$ on a region around the Block 1 cargo core stage. Also shown, the OML of the vehicle (bottom) and the boundaries of the $\Delta C_{p,\mathrm{rms}}$ region (dashed lines) on the OML. For all the Mach numbers: $\alpha = 0$ deg, $\beta = 0$ deg.

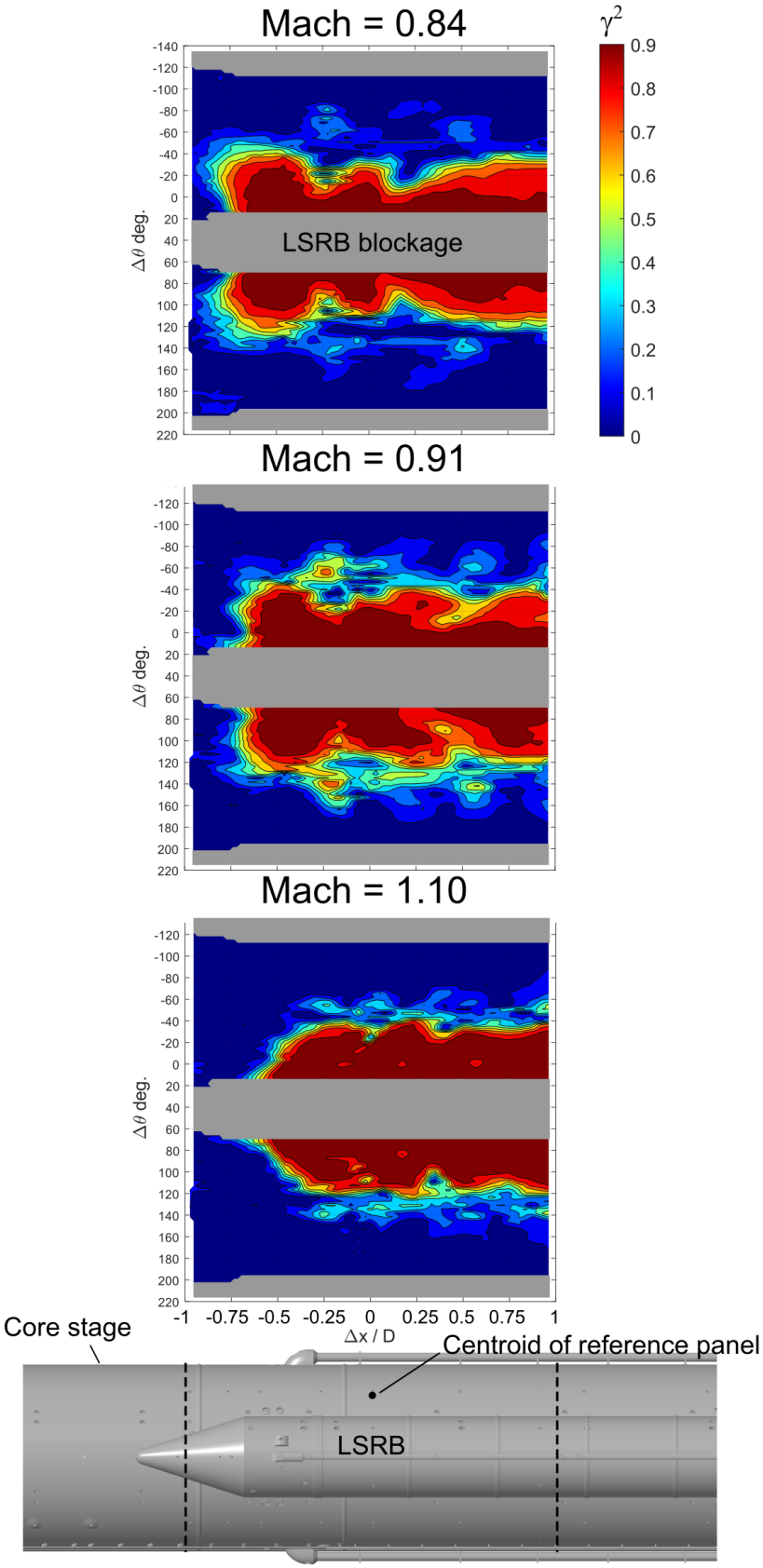


Fig. 8 Distributions of γ^2 at the Strouhal shedding frequency of the forward attachment hardware for a reference panel on the Block 1 cargo core stage. Also shown, the OML of the vehicle (bottom) and the boundaries of the γ^2 coherence region (dashed lines) on the OML. For all the Mach numbers: $\alpha = 0$ deg, $\beta = 0$ deg. Strouhal numbers: Mach = 0.84, St = 0.51 ; Mach = 0.91, St = 0.34 ; Mach = 1.10, St = 0.54.

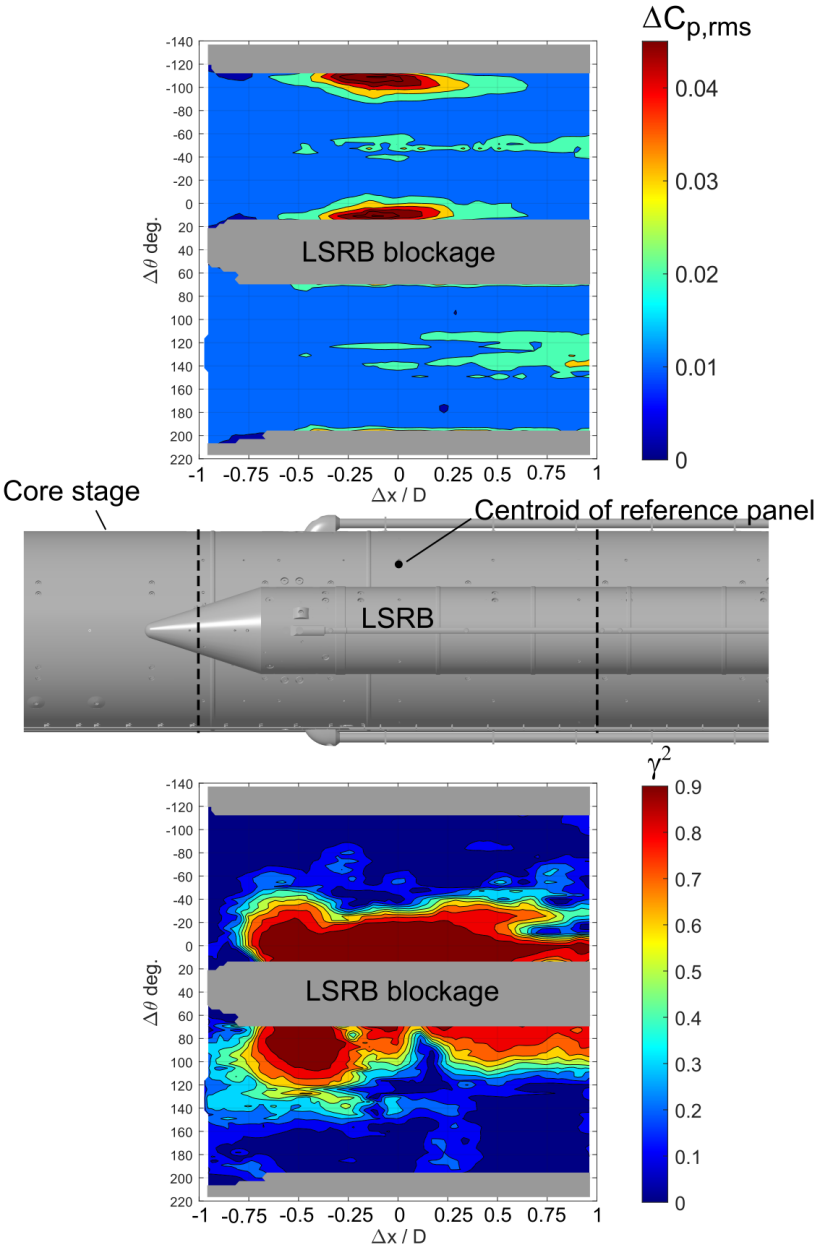


Fig. 9 Distributions of $\Delta C_{p,\mathrm{rms}}$ (top) and γ^2 (bottom) at St = 0.58 for a reference panel on the Block 1 cargo core stage. Also shown, the OML of the vehicle (middle) and the boundaries of the γ^2 coherence region (dashed lines) on the OML for Mach = 0.85, $\alpha = 4$ deg, $\beta = 0$ deg.

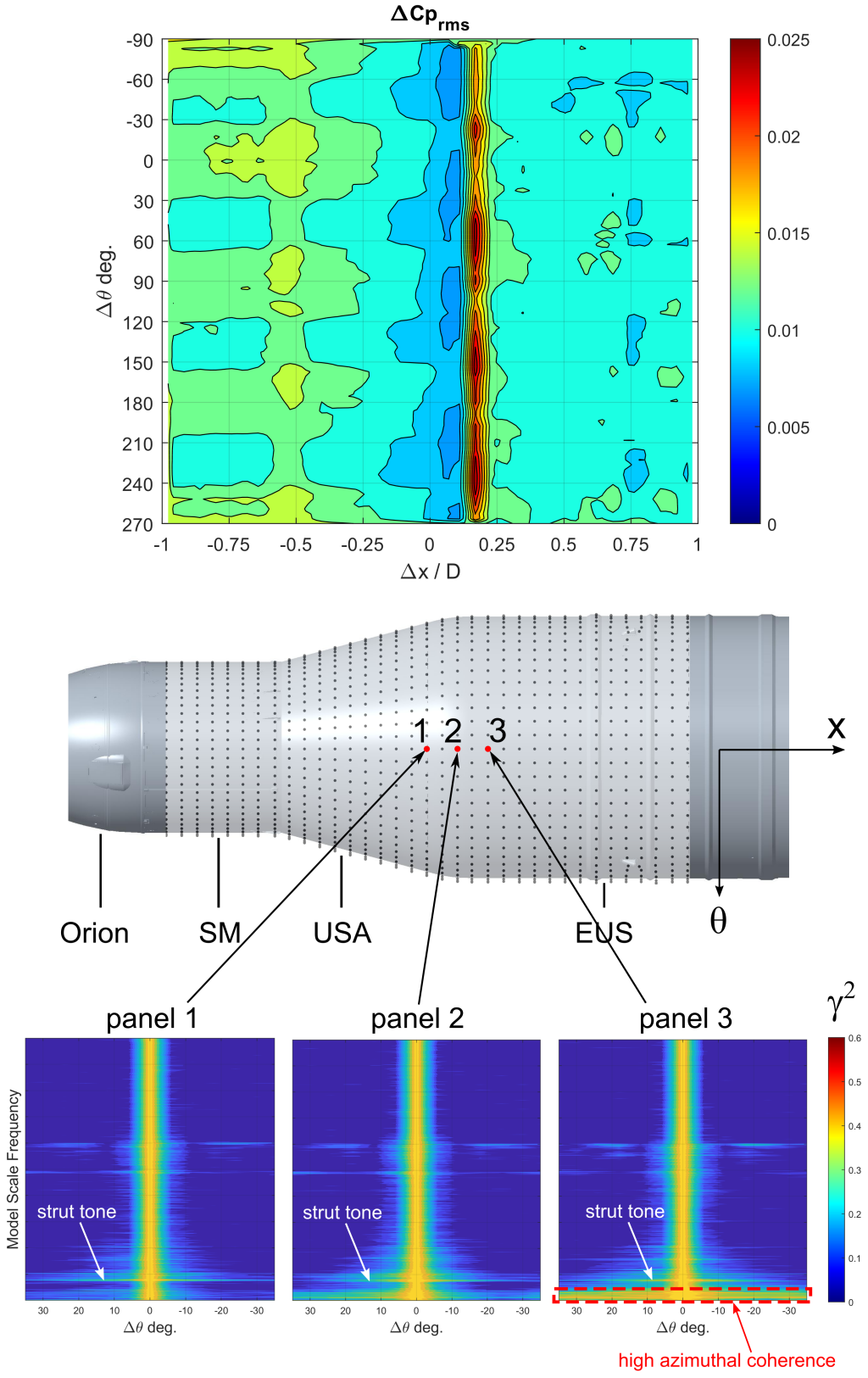


Fig. 10 Bottom charts: contour plots of azimuthal coherence on x = constant planes located in proximity of the Block 1B crew terminal shock near the USA-EUS junction. Reference panel centroids are marked in red on the OML of the vehicle (middle). Top: unwrapped distributions of $\Delta C_{p,\mathrm{rms}}$. Data for Mach = 0.80, $\alpha = 0$ deg, $\beta = 0$ deg.

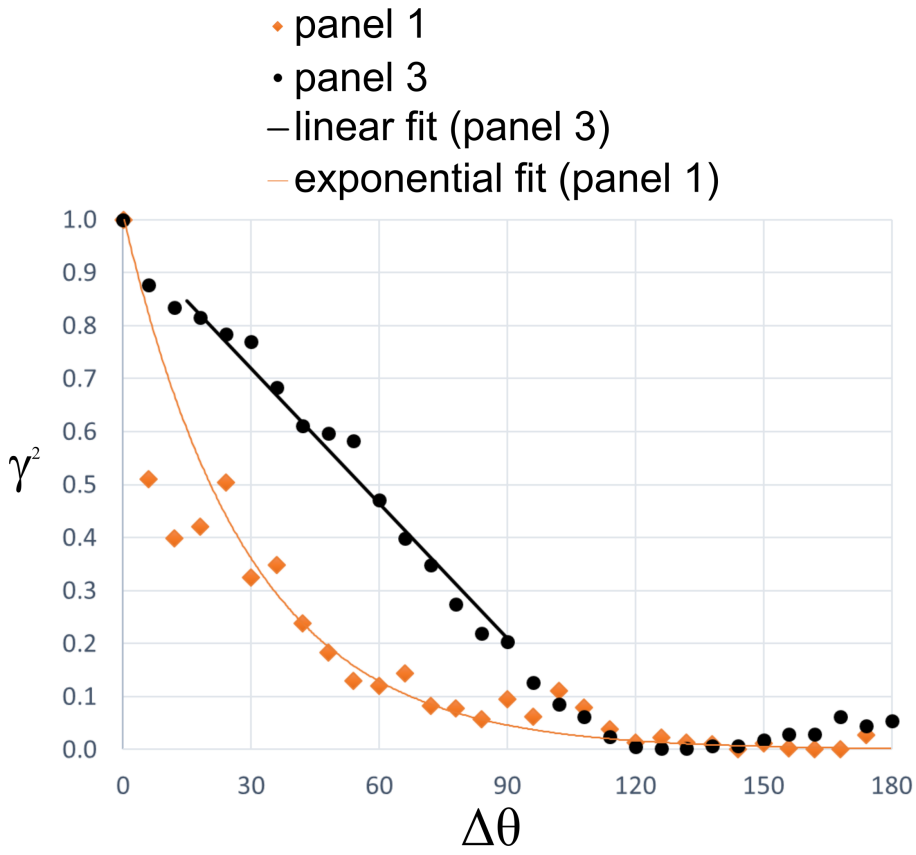


Fig. 11 Azimuthal coherence at St=0.20 for the reference panels of Fig.10. Data for Mach = 0.80, $\alpha = 0$ **deg,** $\beta = 0$ **deg.**

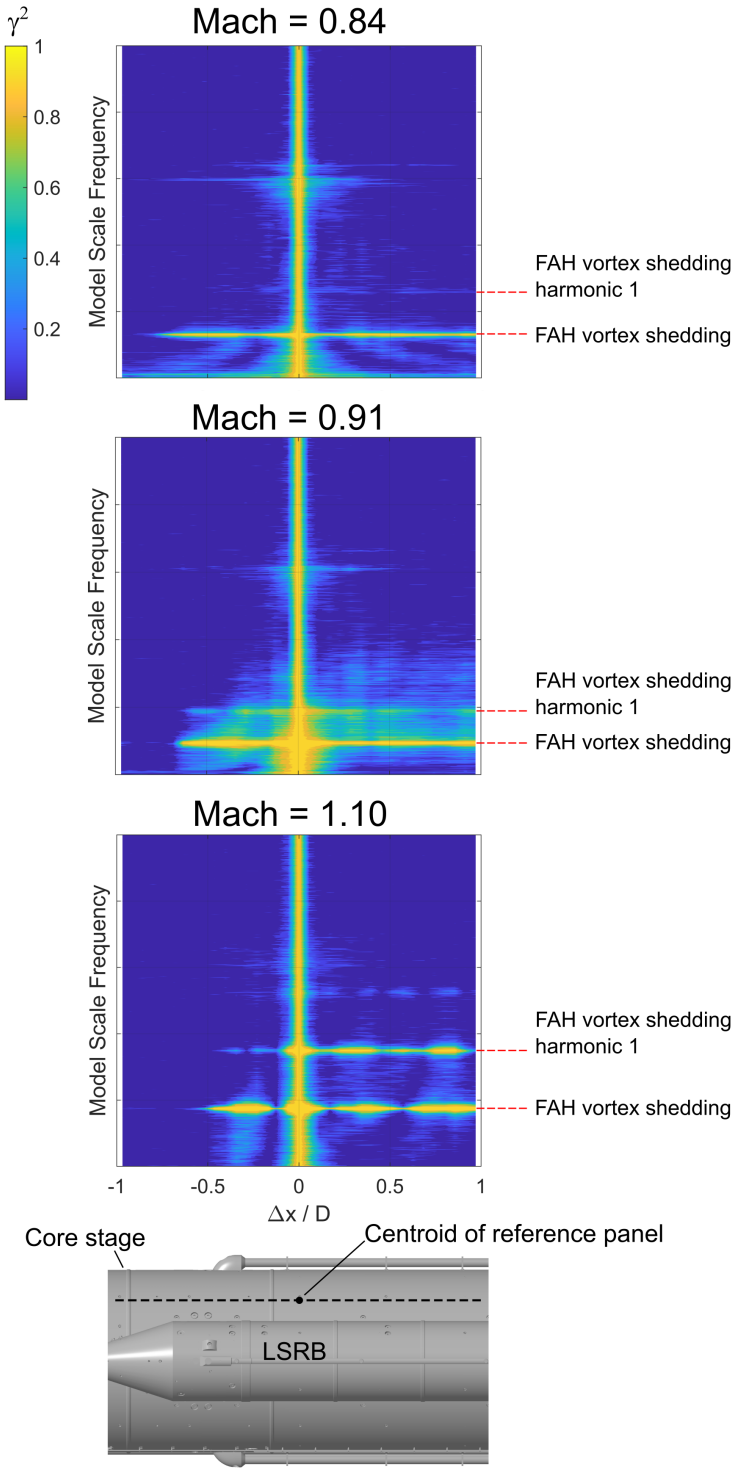


Fig. 12 Distributions of longitudinal γ^2 on a θ = constant plane for a reference panel on the Block 1 cargo core stage. Also shown, the OML of the vehicle (bottom) and the longitudinal segment (dashed line) on the OML where the γ^2 distributions are taken. For all the Mach numbers: $\alpha = 0$ deg, $\beta = 0$ deg.

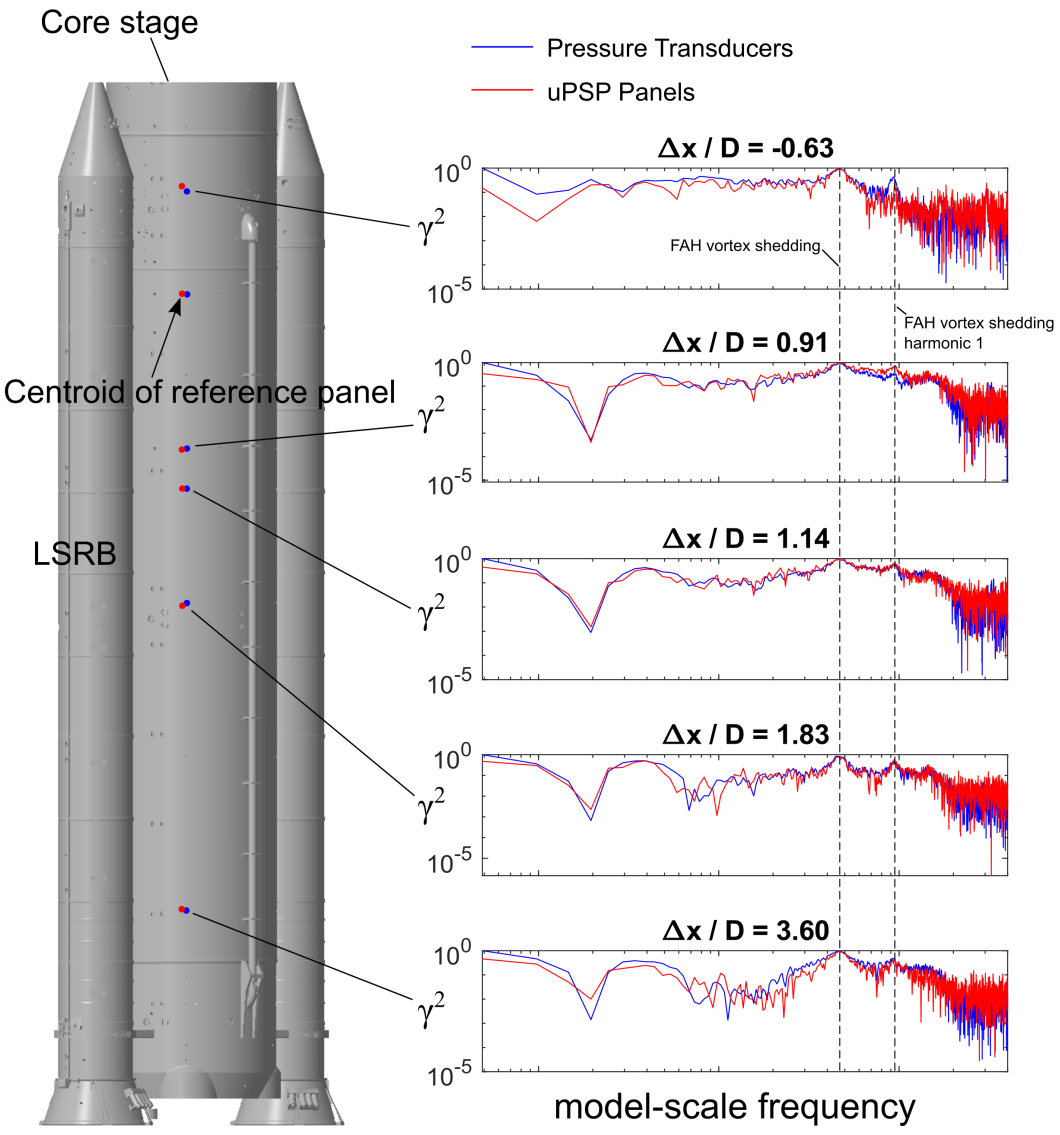


Fig. 13 Magnitude-squared coherence at sample panels on the Block 1 cargo core stage. The OML on the left shows the location of the pressure transducers (blue circles) and the centroids of the nearest uPSP panels (red circles). Comparison between uPSP and PT data for Mach = 0.91, $\alpha = 0$ deg, and $\beta = 0$ deg.

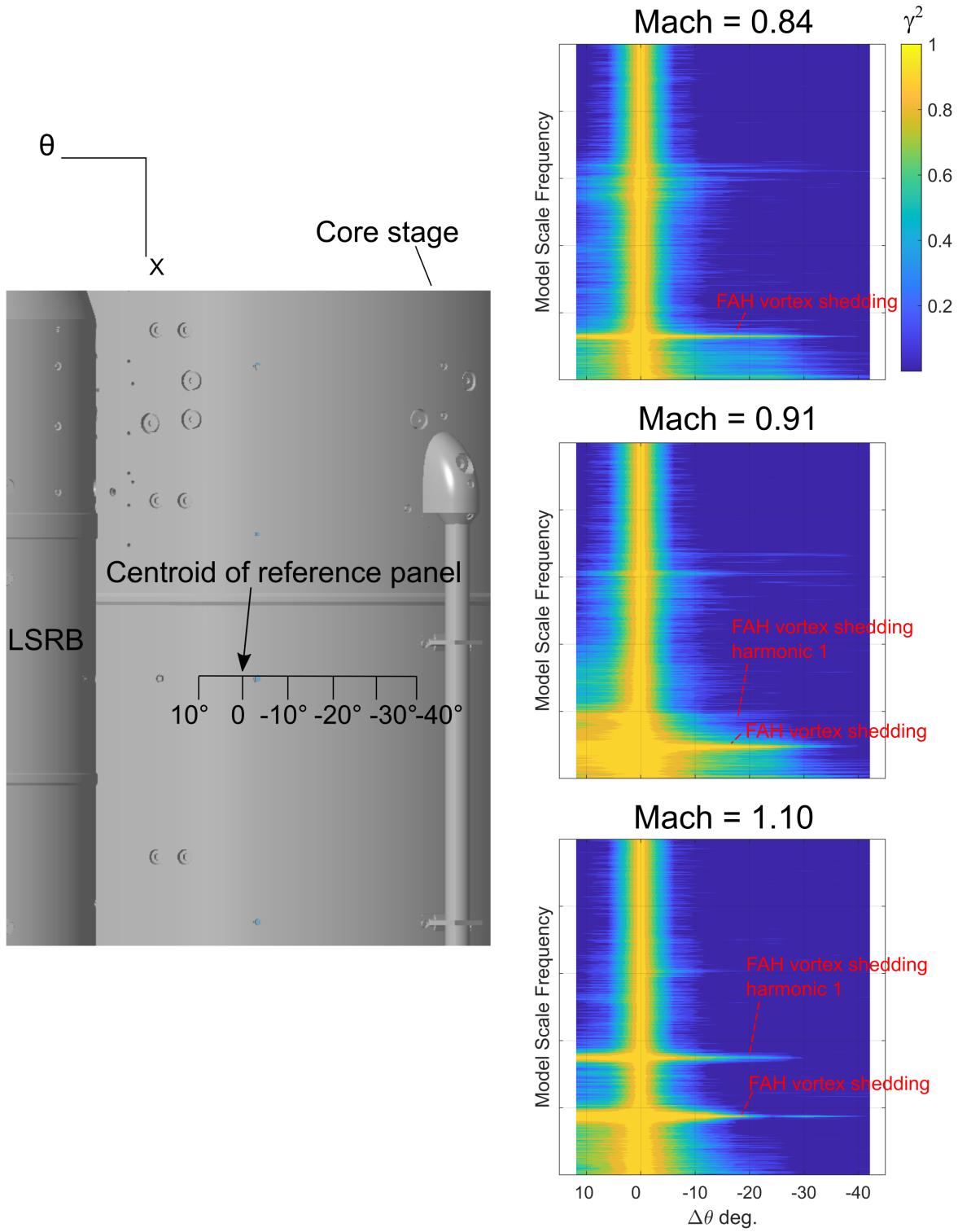


Fig. 14 Distributions of γ^2 on a x = constant plane for a reference panel on the Block 1 cargo core stage. Also shown, the OML of the vehicle (left) and the circular arc on the OML where the γ^2 distributions are taken. For all the Mach numbers: $\alpha = 0$ deg, $\beta = 0$ deg.

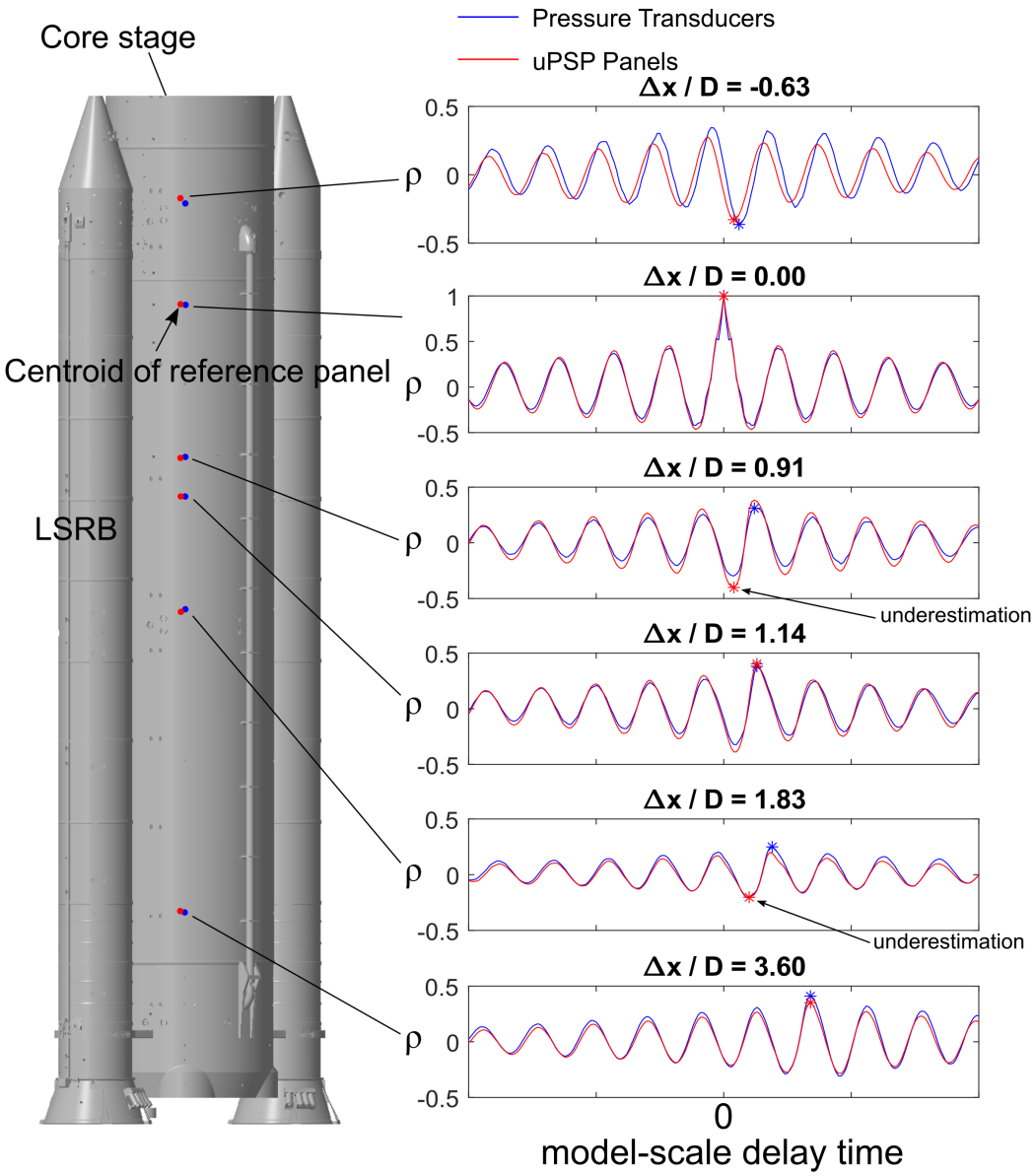


Fig. 15 Cross correlation at sample panels on the Block 1 cargo core stage. The OML on the left shows the location of the pressure transducers (blue circles) and the centroids of the nearest uPSP panels (red circles). Comparison between uPSP and PT data for Mach = 0.91, $\alpha = 0$ deg, and $\beta = 0$ deg.

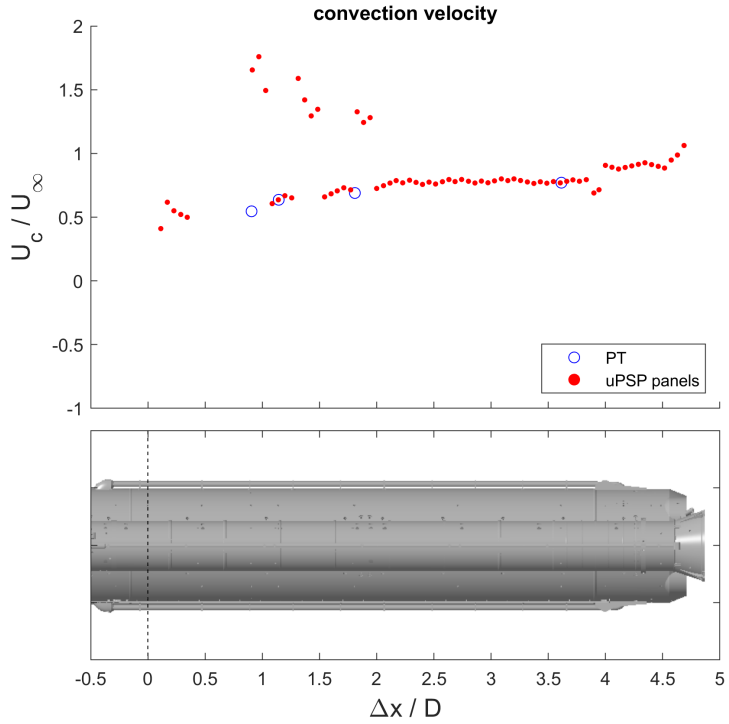


Fig. 16 Convection velocity on the Block 1 cargo core stage for Mach = 0.91, $\alpha = 0$ deg, and $\beta = 0$ deg.

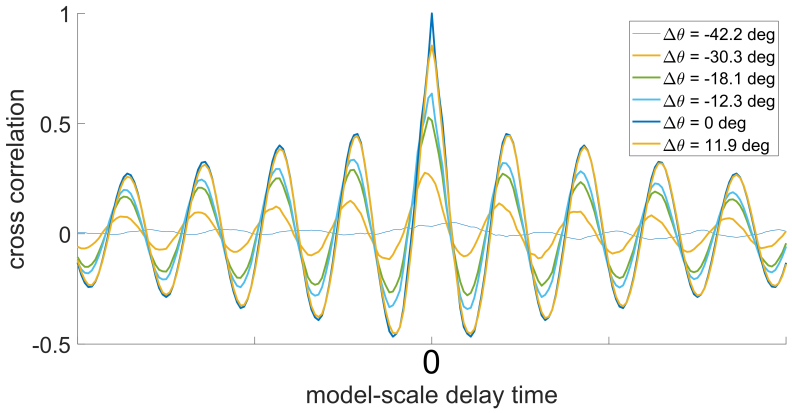


Fig. 17 Azimuthal cross correlation on the Block 1 cargo core stage along the circular arc shown in Fig. 14 for Mach = 0.91, $\alpha = 0$ deg, and $\beta = 0$ deg.

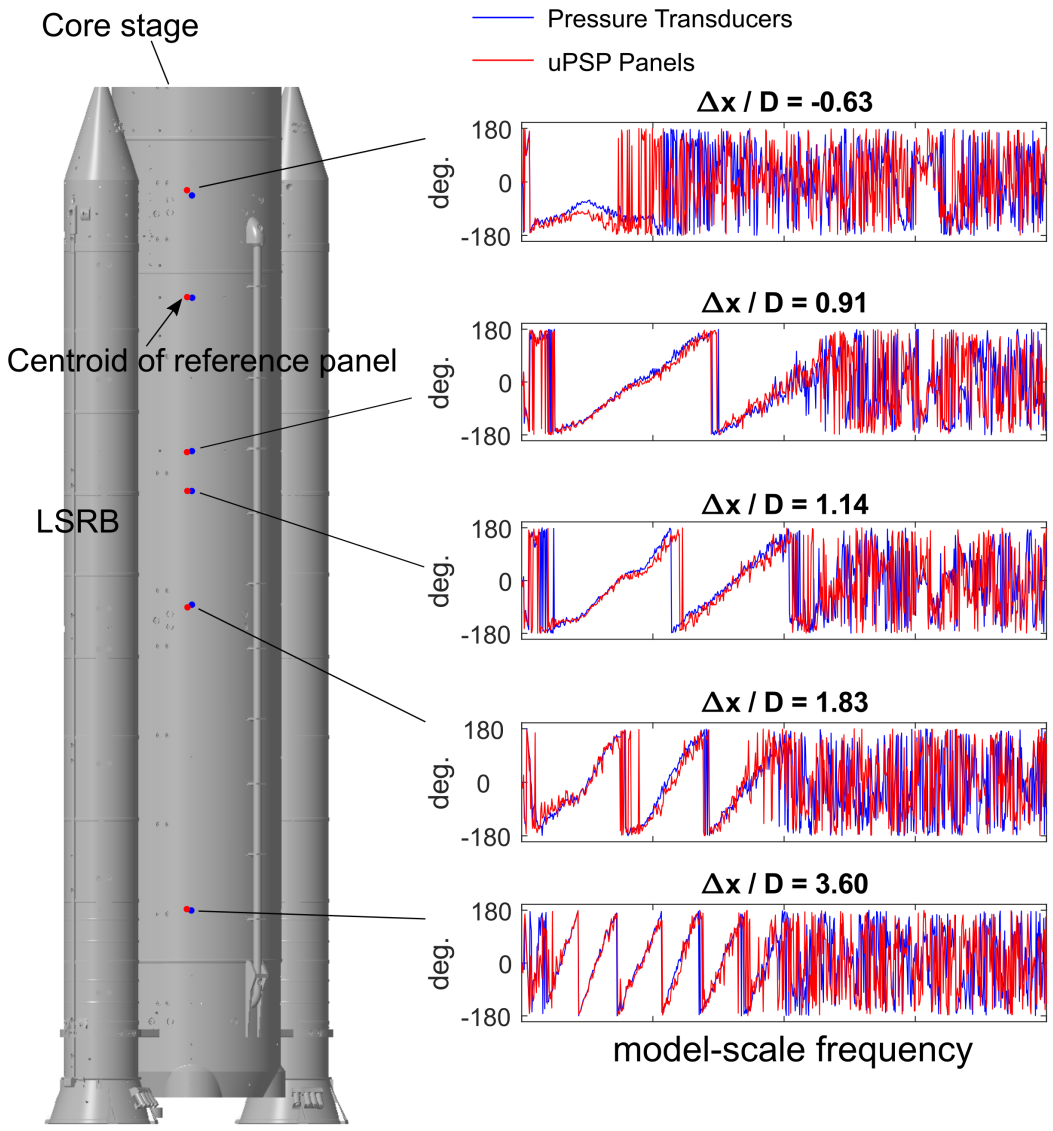


Fig. 18 Cross-spectrum phase angle at sample panels on the Block 1 cargo core stage. The OML on the left shows the location of the pressure transducers (blue circles) and the centroids of the nearest uPSP panels (red circles). Comparison between uPSP and PT data for Mach = 0.91, $\alpha = 0$ deg, and $\beta = 0$ deg.

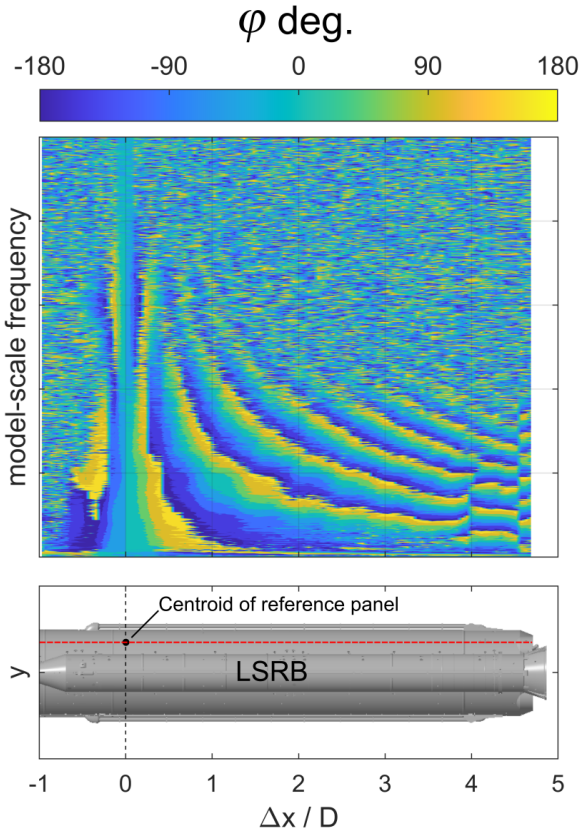


Fig. 19 Cross-spectrum phase angle along a longitudinal segment (red dashed line) on the Block 1 cargo core stage for Mach = 0.91, $\alpha = 0$ deg, and $\beta = 0$ deg.

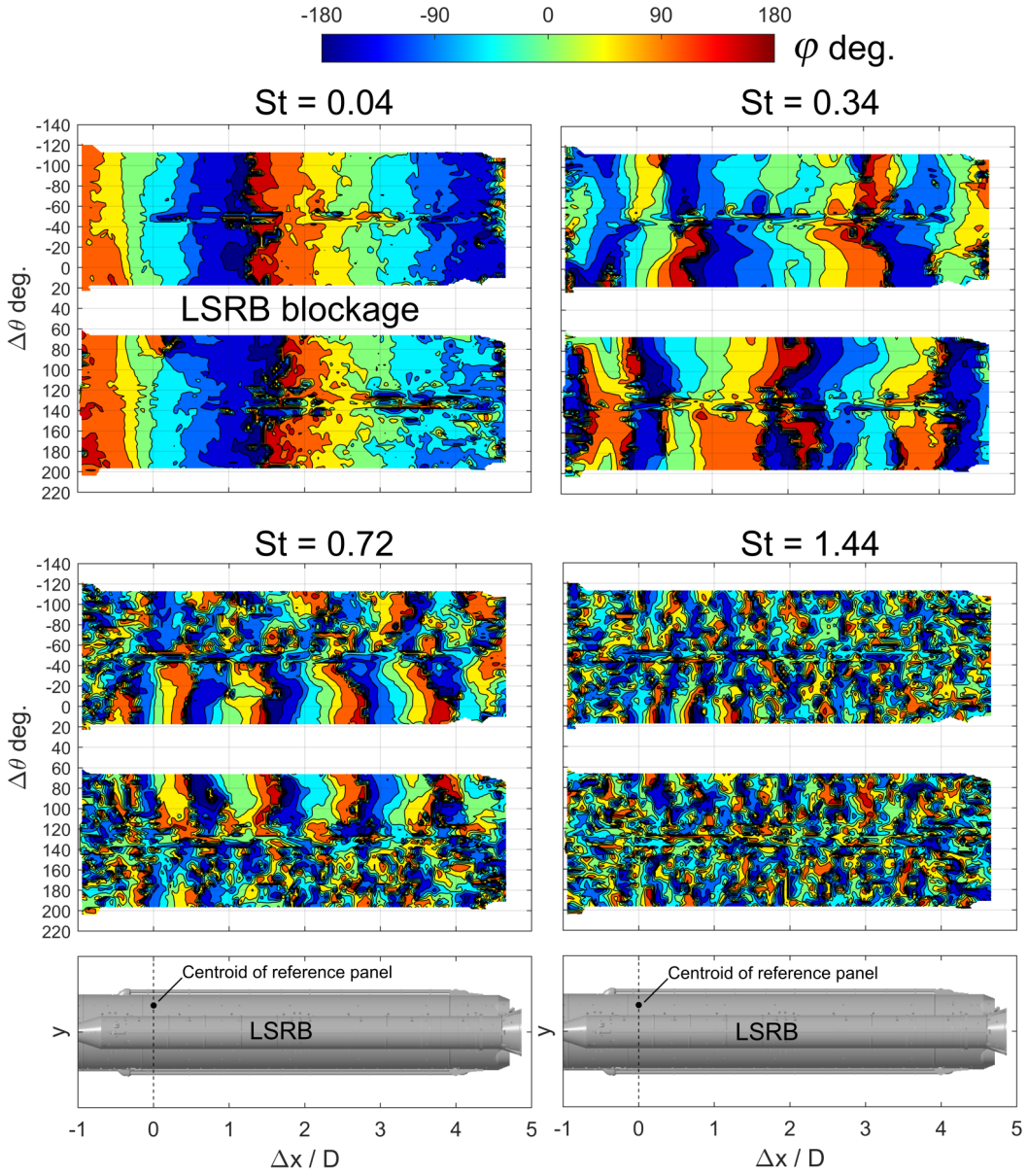


Fig. 20 Cross-spectrum phase angle at sample Strouhal numbers on the Block 1 cargo core stage for Mach = 0.91, $\alpha = 0$ deg, and $\beta = 0$ deg.

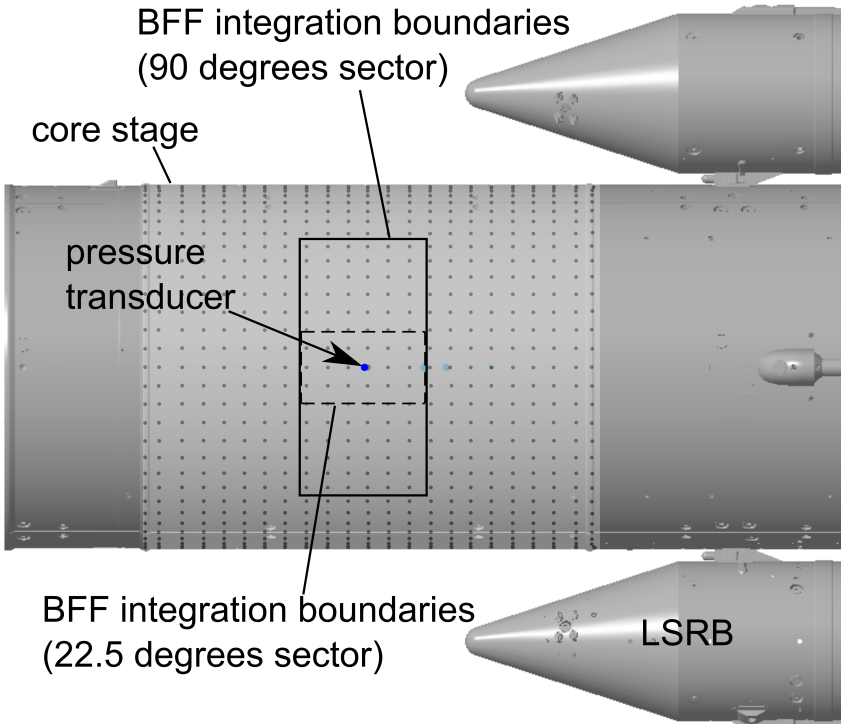


Fig. 21 Selected BFF-integration panels on the Block 1 cargo core stage. Also shown, the centroids of the uPSP panels overlaid on the OML.

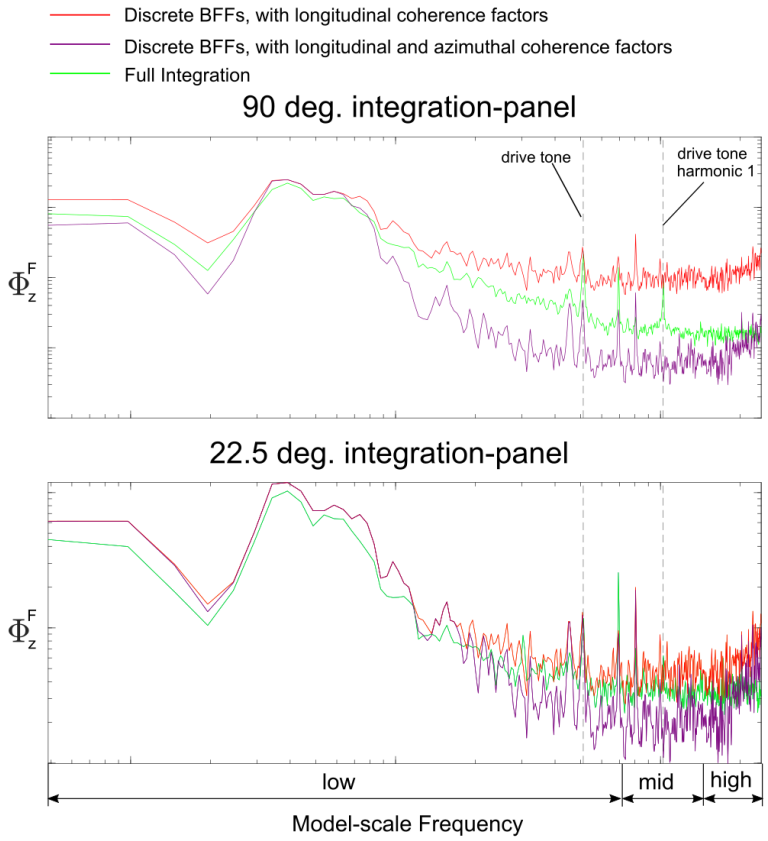


Fig. 22 Power spectral densities of the unsteady force (z-component) on the BFF-integration panels of Fig. 21 for Mach = 0.91, $\alpha = 0$ deg, and $\beta = 0$ deg.

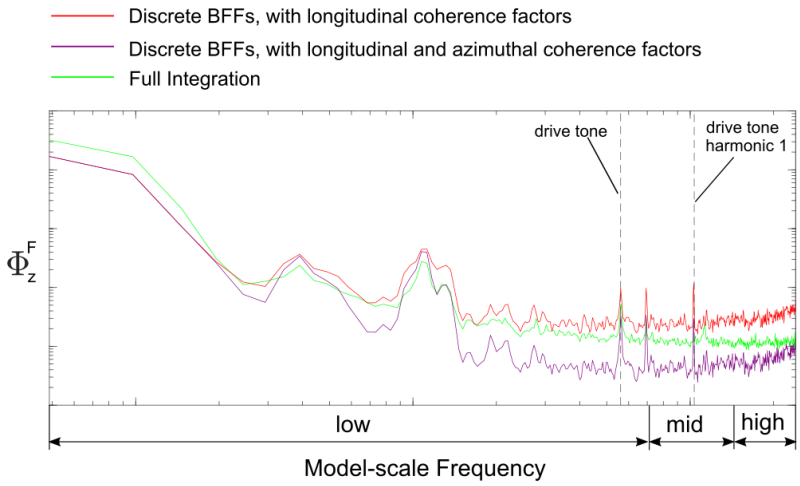


Fig. 23 Power spectral densities of the unsteady force (z-component) on the BFF-integration panels of Fig. 5 for Mach = 0.95, $\alpha = 0$ deg, and $\beta = 0$ deg.

Acknowledgment

The authors would like to thank the uPSP test team at the NASA Ames Research Center, to include Nettie Roozeboom, Jennifer Baerny, Jie Li, David Murakami, Marc Shaw-Lecerf, Paul Stremel, and Lucy Tang and also Jessica Powell at the NASA Johnson Space Center for their invaluable assistance in acquiring, processing, and discussing the uPSP data analyzed in this paper. Also, the authors would like to thank Derek Dalle of the NASA Ames Research Center for providing the CFD data presented in this paper, and Craig Streett of the NASA Langley Research Center for reviewing the paper and for his helpful comments.

References

[1] Piatak, D. J., Sekula, M. K., and Rausch, R. D., "Ares Launch Vehicle Transonic Buffet Testing and Analysis Techniques," *Journal of Spacecraft and Rockets*, Vol. 49, No. 5, 2012, pp. 798–807. doi:10.2514/1.A32175, URL https://doi.org/10.2514/1.A32175.

[2] Piatak, D. J., Sekula, M. K., and Rausch, R., *Sensitivity of Space Launch System Buffet Forcing Functions to Buffet Mitigation Options*, 2016. doi:10.2514/6.2016-0544, URL https://arc.aiaa.org/doi/abs/10.2514/6.2016-0544.

[3] Sekula, M. K., Piatak, D. J., and Rausch, R., *Effect of Surface Pressure Integration Methodology on Launch Vehicle Buffet Forcing Functions*, 2016. doi:10.2514/6.2016-0545, URL https://arc.aiaa.org/doi/abs/10.2514/6.2016-0545.

[4] Panda, J., "Experimental Verification of Buffet Calculation Procedure Using Unsteady Pressure-Sensitive Paint," *Journal of Aircraft*, Vol. 54, No. 5, 2017, pp. 1791–1801. doi:10.2514/1.C033917, URL https://doi.org/10.2514/1.C033917.

[5] Ramey, J. M., Sekula, M. K., Piatak, D. J., Heaney, P. S., and Soranna, F., "Development of Buffet Forcing Functions using Frequency-Dependent Coherence Factors," *AIAA SciTech 2021 Forum*, 2021.

[6] Roozeboom, N., Powell, J., Baerny, J., Murakami, D., Ngo, C., Garbeff, T. J., Ross, J. C., and Flach, R., *Development of Unsteady Pressure-Sensitive Paint Application on NASA Space Launch System*, 2019. doi:10.2514/6.2019-3502, URL https://arc.aiaa.org/doi/abs/10.2514/6.2019-3502.

[7] Sekula, M. K., Piatak, D. J., Rausch, R. D., Ross, J. C., and Sellers, M. E., *Assessment of Buffet Forcing Function Development Process Using Unsteady Pressure Sensitive Paint*, 2019. doi:10.2514/6.2019-3503, URL https://arc.aiaa.org/doi/abs/10.2514/6.2019-3503.

[8] Soranna, F., Heaney, P. S., Sekula, M. K., Piatak, D. J., Ramey, J. M., Roozeboom, N. H., Murakami, D. D., Baerny, J. K., Stremel, P. M., Jessica, J. L., and Powell, M., "Analysis of Buffet Forcing Functions Estimated from Unsteady Pressure Sensitive Paint," *AIAA Aviation 2020 Forum*, 2020.

[9] Powell, J. M., Murman, S. M., Ngo, C., Roozeboom, N., Murakami, D. D., Baerny, J. K., and Lie, J., *Development of Unsteady-PSP Data Processing and Analysis Tools for the NASA Ames Unitary 11ft Wind Tunnel*, 2020. doi:10.2514/6.2020-0292, URL https://arc.aiaa.org/doi/abs/10.2514/6.2020-0292.

[10] Heaney, P. S., Soranna, F., Sekula, M. K., Piatak, D. J., and Ramey, J. M., "Analysis of Transonic Unsteady Aerodynamic Environments using Unsteady Pressure Sensitive Paint for the Space Launch System Block 1 Cargo Launch Vehicle," *AIAA SciTech 2021 Forum*, 2021.

[11] Singer, B. A., "Turbulent Wall-Pressure Fluctuations: A New Model for Off-Axis Cross-Spectral Density," *J. Fluids Eng.*, Vol. 119, No. 2, 1997, pp. 277–280.

[12] Andreopoulos, Y., Agui, J. H., and Briassulis, G., "Shock Wave—Turbulence Interactions," *Annual Review of Fluid Mechanics*, Vol. 32, No. 1, 2000, pp. 309–345. doi:10.1146/annurev.fluid.32.1.309, URL https://doi.org/10.1146/annurev.fluid.32.1.309.

[13] Corcos, G. M., "Resolution of Pressure in Turbulence," *Acoustical Society of America Journal*, Vol. 35, No. 2, 1963, p. 192. doi:10.1121/1.1918431.

[14] Panda, J., Roozeboom, N. H., and Ross, J. C., "Wavenumber-Frequency Spectra on a Launch Vehicle Model Measured via Unsteady Pressure-Sensitive Paint," *AIAA Journal*, Vol. 57, No. 5, 2019, pp. 1801–1817. doi:10.2514/1.J057449, URL https://doi.org/10.2514/1.J057449.

[15] Heaney, P. S., Sekula, M. K., Piatak, D. J., Ramey, J. M., and Soranna, F., *Evaluation of Preliminary Buffet Forcing Function Development based on Wind-Tunnel Tests of Geometrically-similar Models*, 2020. doi:10.2514/6.2020-2669, URL https://arc.aiaa.org/doi/abs/10.2514/6.2020-2669.

[16] Bremner, P., Blelloch, P., Hutchings, A., Shah, P., Streett, C., and Larsen, C., *Validation of Methods to Predict Vibration of a Panel in the Near Field of a Hot Supersonic Rocket Plume*, 2011. doi:10.2514/6.2011-2852, URL https://arc.aiaa.org/doi/abs/10.2514/6.2011-2852.

[17] Taylor, G. I., "The Spectrum of Turbulence," *Proceedings of the Royal Society A: Mathematical, Physical and Engineering Sciences*, Vol. 164, No. 919, 1938, pp. 476–490. doi:10.1098/rspa.1938.0032, URL https://royalsocietypublishing.org/doi/abs/10.1098/rspa.1938.0032.

[18] Moin, P., "Revisiting Taylor's hypothesis," *Journal of Fluid Mechanics*, Vol. 640, 2009, p. 1–4. doi:10.1017/S0022112009992126.